

AD/A-003 584

CARBON MONOXIDE LASER

R. E. Center, et al

Avco Everett Research Laboratory,
Incorporated

Prepared for:

Advanced Research Projects Agency
Office of Naval Research

January 1975

DISTRIBUTED BY:

NTIS

National Technical Information Service
U. S. DEPARTMENT OF COMMERCE

UNCLASSIFIED

Security Classification

AD/A-003584

DOCUMENT CONTROL DATA - R & D

(Security classification of title, body of abstract and indexing annotation must be entered when the overall report is classified)

1. ORIGINATING ACTIVITY (Corporate author) AVCO EVERETT RESEARCH LABORATORY, INC. 2385 Revere Beach Parkway Everett, Massachusetts 02149		2a. REPORT SECURITY CLASSIFICATION UNCLASSIFIED	
		2b. GROUP	
3. REPORT TITLE CARBON MONOXIDE LASER			
4. DESCRIPTIVE NOTES (Type of report and inclusive dates) Annual Technical Report			
5. AUTHOR(S) (First name, middle initial, last name) R. E. Center and M. J. W. Boness			
6. REPORT DATE January 1975		7a. TOTAL NO OF PAGES 65	7b. NO OF REFS 25
8a. CONTRACT OR GRANT NO N00014-72-C-0030		8b. ORIGINATOR'S REPORT NUMBER(S) Annual Technical Report	
b. PROJECT NO		9b. OTHER REPORT NO(S) (Any other numbers that may be assigned this report)	
c.			
d.			
10. DISTRIBUTION STATEMENT Approved for public release; distribution unlimited.			
11. SUPPLEMENTARY NOTES		12. SPONSORING MILITARY ACTIVITY ARPA, DoD, ARPA Order No. 1807, Code No. 421 and monitored by ONR, Arlington, Virginia.	
13. ABSTRACT <p>The main objective of this program is the investigation of the pulsed electrical CO laser to determine the relative scaling parameters and the usefulness of high power CO lasers in systems applications. The current contract has included measurements of small signal gain on varying vibrational and rotational transitions, operation with an unstable resonator and the design fabrication and assembly of an entirely new transverse flow system together with a new heat exchanger.</p> <p>Small signal gains of up to 4 1/2% per cm were measured. Maximum gain was observed on the 9P(10) and the 8P(10) transitions. The measurements were compared with parametric performance predictions derived from kinetic modeling calculations. The experimental data agreed qualitatively with the modeling calculations. Some measurements on low transitions in particular, 6P(10) and 5P(13) support the hypothesis that resonant absorption by overlapping transitions can seriously suppress gain on certain lines. This mechanism will play an important role in determining the spectral distribution and hence the atmospheric transmission properties of the high pressure carbon monoxide electric discharge laser.</p> <p>The new flow system discharge cavity and heat exchanger have been designed with the aim of obtaining a near diffraction limited beam from the pulsed CO laser. The design considerations are described in detail in the present report. The new system uses transverse flow in order to obtain the maximum flow velocity which directed vertically upwards to ensure that buoyancy effects are favorable.</p>			

DD FORM 1473
1 NOV 66Reproduced by
NATIONAL TECHNICAL
INFORMATION SERVICE
U S Department of Commerce
Springfield VA 22151UNCLASSIFIED
Security Classification

CARBON MONOXIDE LASER

by

R. E. Center and M. J. W. Boness

ANNUAL TECHNICAL REPORT

AVCO EVERETT RESEARCH LABORATORY, INC.
a Subsidiary of Avco Corporation
Everett, Massachusetts

January 1975

prepared for

ADVANCED RESEARCH PROJECTS AGENCY
DEPARTMENT OF DEFENSE
ARPA Order No. 1807
Code No. 421

and

monitored by

OFFICE OF NAVAL RESEARCH
Arlington, Virginia
under Contract No. N00014-72-C-0030

APPROVED FOR PUBLIC RELEASE; DISTRIBUTION UNLIMITED.

if

FOREWORD

ARPA Order No.: 1807

Program Code No.: 421

Contract No.: N00014-72-C-0030

Principal Investigator: R. E. Center
Telephone No.: (617) 389-3000, Ext. 593

Effective Date of Contract: November 1, 1971

Contract Expiration Date: June 30, 1975

Amount of Contract: \$884,079

Scientific Officer: Director, Physics Program, Physical Sciences Division,
Office of Naval Research, Department of the Navy,
800 North Quincy Street, Arlington, Virginia 22217

Short Title of Work: CO Laser

ABSTRACT

The main objective of this program is the investigation of the pulsed electrical CO laser to determine the relative scaling parameters and the usefulness of high power CO lasers in systems applications. The current contract has included measurements of small signal gain on varying vibrational and rotational transitions, operation with an unstable resonator and the design fabrication and assembly of an entirely new transverse flow system together with a new heat exchanger.

Small signal gains of up to $4 \frac{1}{2} \%$ per cm were measured. Maximum gain was observed on the $9 P(10)$ and the $8 P(10)$ transitions. The measurements were compared with parametric performance predictions derived from kinetic modelling calculations. The experimental data agreed qualitatively with the modelling calculations. Some measurements on low transitions in particular, $6 P(10)$ and $5 P(13)$ support the hypothesis that resonant absorption by overlapping transitions can seriously suppress gain on certain lines. This mechanism will play an important role in determining the spectral distribution and hence the atmospheric transmission properties of the high pressure carbon monoxide electric discharge laser.

The new flow system discharge cavity and heat exchanger have been designed with the aim of obtaining a near diffraction limited beam from the pulsed CO laser. The design considerations are described in

detail in the present report. The new system uses transverse flow in order to obtain the maximum flow velocity which is directed vertically upwards to ensure that buoyancy effects are favorable.

TABLE OF CONTENTS

<u>Section</u>	<u>Page</u>
Foreword	ii
Abstract	iii
List of Illustrations	vii
I INTRODUCTION	1
II GAIN MEASUREMENTS	3
A. Technique	3
B. Probe Laser Construction	4
C. Spectral Output	7
D. Results	10
III UNSTABLE RESONATOR	21
IV WATER VAPOR ABSORPTION CELL	25
V NEW DISCHARGE CAVITY/FLOW SYSTEM	29
A. Boundary Layer Calculations	31
B. Design of Heat Exchanger	42
C. Discharge Electrode Configuration	47
D. Fabrication and Testing	53
REFERENCES	55

LIST OF ILLUSTRATIONS

<u>Figure</u>		<u>Page</u>
1	Details of the Construction of the Probe Laser	5
2	Measurements of Maximum Small Signal Gain as Functions of Terminal Rotational Level for Various P Branch Vibrational Transitions	11
3	Temporal Variation of the Probe Laser Intensity Operating on the 5P (13) Transition for Different Values of E/N	13
4	Predictions of Maximum Small Signal Gain for Various P Branch Transitions	15
5	Predictions of the Temporal Variation of Small Signal Gain for the P (12) Line of Various Vibrational Bands	16
6	Temporal Variation of the Probe Laser Intensity while Oscillating on the 6P (10) and 9P (9) Transitions	18
7	Theoretical and Experimental Values of the Time to Reach Threshold Gain as Functions of the Upper Vibrational Level P (12) Transition	19
8	The Near Field Burn Pattern Obtained Using the Unstable Resonator Configuration	23
9	Schematic of the Water Vapor Absorption Cell	26
10	Schematic of Transverse Flow/Discharge Cavity System	30
11	Scaling Lengths vs Flow Velocity, u_∞ , and the Gas Temperature T_∞ for CO-N ₂ Mixtures and 300°K Wall Temperature	39
12	Laminar boundary layer results (Ref. 2) in CO-N ₂ mixtures for $\Delta\ell$ vs the downstream distance from the leading edge, x	40
13	Turbulent boundary layer results, Eqs. (14) and (15), in CO-N ₂ mixtures for $\Delta\ell$ vs the downstream distance from the leading edge, x	41

<u>Figure</u>		<u>Page</u>
14	Schematic of the Porous Plate Heat Exchanger	43
15	Potential Distribution in Cavity Neglecting Nonuniform Ionization	50
16	Potential Distribution Assuming Ionization Rate Eq. (35)	51
17	Distribution of Electrical Energy Deposition in Cavity	52

I. INTRODUCTION

The CO laser program is directed toward the investigation of the performance characteristics of the pulsed electrical CO laser using an electron beam sustained discharge. The experimental investigation is aimed at evaluating the scaling parameters of high power electrical CO lasers and their potential systems applications. The overall program includes theoretical modelling to provide support for the design of the experiment and the interpretation of the data.

The following areas of investigation were included in the current contract.

- 1) Measurements of the temporal variation of the small signal gain over the entire range of accessible transitions.
- 2) Operation with an unstable resonator over the central region of the original discharge cavity.
- 3) Design and construction of an intracavity water vapor absorption cell.
- 4) Design and construction of a new flow system/discharge cavity and heat exchanger for operation over the temperature from 80°K to 300°K and gas densities of the order of 1 amagat with the design goal of achieving better than 1 1/2 times the diffraction limited beam.

The small signal gain measurements are described in detail in the present report and are compared with parametric performance

predictions derived from the AERL kinetic model. Maximum gains of $4 \frac{1}{2} \%$ per cm were measured on two transitions. Anomalous behavior was observed on several low lying transitions. These transitions exhibited oscillating gain/absorption behavior or in some cases only absorption where gain had been predicted. The measurements can be interpreted when allowance is made for overlapping transitions which results in gain suppression on several lines. These overlaps will play an important role in determining spectral distribution of the high pressure carbon monoxide electric discharge laser and will influence the atmospheric transmission properties of the system. Lasing operation with the unstable resonator cavity indicated nonuniform energy deposition across the discharge.

The new flow system/discharge cavity has been designed for transverse flow operation directed vertically upwards. This is to ensure that buoyancy effects are favorable and to minimize the boundary layer growth on the room temperature side walls. A porous plate heat exchanger system has been designed and constructed with large thermal mass to provide the order of 10 sec flow operation of the mass flow of 150 grams per sec. The discharge cavity is designed to be compatible with the existing 20 cm x 100 cm electron beam.

II. GAIN MEASUREMENTS

Measurements of small signal gain have been performed in the 20 liter E-beam sustained CO laser and the results compared with parametric performance predictions⁽³⁾ derived from kinetic modelling calculations.⁽¹⁾ Maximum gain of $4\frac{1}{2}\%$ /cm was measured on the 9P(10) and 8P(10) transitions. The measurements support the hypothesis⁽²⁾ that resonance absorption by overlapping transitions is the mechanism responsible for gain suppression on certain lines. This mechanism will play an important role in determining the spectral distribution, and hence the atmospheric transmission properties of the high pressure carbon monoxide electric discharge laser.

A. TECHNIQUE

The technique is conceptually simple. A C. W. CO probe laser beam was transmitted through the active discharge volume of the 20 liter E-beam sustained CO laser. The cavity mirrors were removed to prevent oscillation. The laser⁽³⁾ was operated at an initial gas temperature of 130°K , a density of $1/3$ Amagat and with a gas composition 20% CO = 80% N_2 . The electric field initially 13 KV/cm/atm decayed to approximately 10 KV/cm/atm by the end of the $60\ \mu\text{sec}$ current pulse. The voltage droop was associated with discharging the capacitor bank supplying the energy to the electric field.

B. PROBE LASER CONSTRUCTION

Considerable attention was paid to the design of the probe laser to ensure high output stability. Details of the probe laser construction are shown in Figure 1. The laser consisted of a 150 cm long thick walled pyrex tube with a 1.35 cm i. d. The electrodes, formed from high purity nickel, were mounted in side arms and located one near each end and one at the center of the discharge tube.

Special care was taken in mounting the electrodes to prevent the discharge seeing the edges of the nickel cylinders, thus reducing the formation of hot spots and significantly improving the stability of the discharge. This design also suppresses sputtering from the outer electrode surface onto the glass enclosure reducing chemical degradation of the gas composition. The flowing gas mixture, $\text{He:N}_2:\text{CO}$, 10:1:0.3 torr was pumped by a 15 c. f. m. fore pump.

The conventional method of providing liquid nitrogen cooling to the discharge tube by circulating the coolant in a concentric glass jacket was not adopted. This technique may degrade the performance of the laser due to mechanical vibration associated with circulating the coolant. Temperature variation along the discharge tube may also occur as a consequence of gas pressure gradients in the jacket introducing variations in the temperature of the liquid nitrogen.

Instead, the discharge tube was immersed in a large volume bath of freely evaporating liquid nitrogen which obviated both problems associated with the concentric cooling jacket scheme. The bath consisted of a 1/2 mil thick aluminized mylar foil bag sealed onto the ends of the tube with

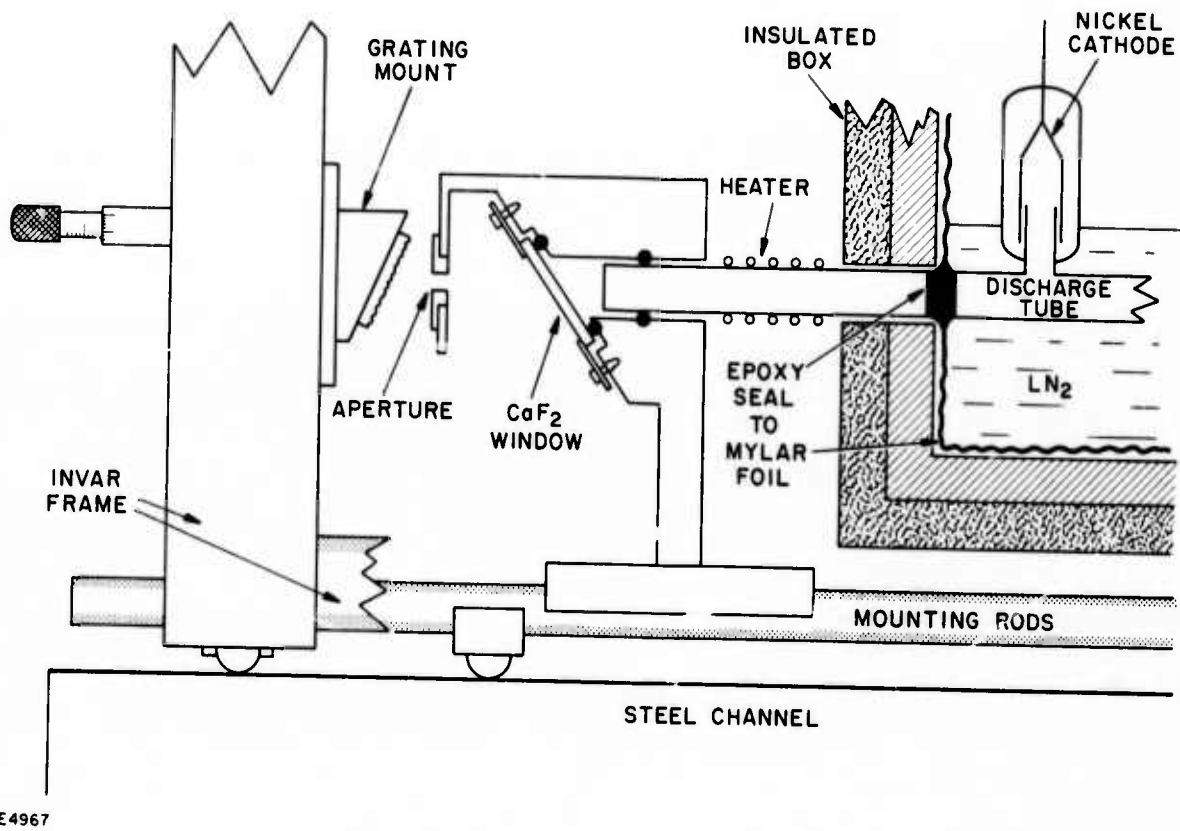


Figure 1 Details of the Construction of the Probe Laser

a low temperature epoxy cement. The bag was formed and supported by a rectangular wooden box insulated with a styrofoam lining. The ends of the discharge tube exterior to the bath were terminated with Brewster angle calcium fluoride windows. Vacuum integrity was maintained by viton O-ring seals between aluminum supports and the discharge tube and windows. Heater tapes wound around the discharge tube between the bath and the window holders prevented excessive cooling of the O-ring seals and maintained the windows at room temperature to avoid problems of condensation. The laser cavity was formed by a 4 meter radius 95% transmitting germanium mirror and an original grating blazed at 5.4μ with 360 lines/inch. Both elements were placed in gimbal mounts with micrometer tilt adjustments and equipped with piezo electric drives to provide longitudinal mode tuning. The mounts were each bolted to massive invar plates separated at their four corners by 2" diameter invar rods, thus providing a high degree of thermal and mechanical stability for the laser cavity. The invar frame was further supported on a 12" x 3" steel channel which also carried ground steel rods which formed on optical bench for supporting the aluminum window mounts. Finally, the channel was mechanically isolated from the surroundings with an auto-vibration mounting.

The laser was excited by a dc discharge. Power was provided from a current regulated power supply typically operating at 15 kV and supplying 10 mA through 500 k Ω ballast resistors connected to each cathode.

Single transverse mode oscillation was achieved using an intra cavity 6 mm diameter aperture placed close to the diffraction grating. Beyond the cavity the optical path was defined by a 6 mm diameter iris after which typical line intensities of 100 - 300 mW were obtained.

C. SPECTRAL OUTPUT

The wavelengths of the lasing transitions were measured with a 1/2 meter Jarrel-Ash monochromator equipped with a 295 lines/mm grating blazed at 3.7μ used in conjunction with a Au-Ge Detector. The monochromator was calibrated with mercury lines in high order. Using 100μ slits, the accuracy of the instrument at 2000 cm^{-1} was $\pm 0.5 \text{ cm}^{-1}$.

The wavelengths of 50 P branch transitions for the first 25 vibrational levels were calculated using the expression for the energy levels of the anharmonic oscillator and the values of the spectroscopic constants for the CO molecule recently determined by Eng et al. ⁽⁴⁾

The line separation within a vibrational band is typically 4 cm^{-1} , the calculated wavelengths are believed correct to within 10^{-4} cm^{-1} . Thus, correct line identification is normally assured. Occasional difficulties are associated with overlapping lines encountered at the band extremities; however, this difficulty could be resolved by noticing variation between the spacings of lines belonging to different bands. The identification was confirmed by predicting the identity of two missing transitions in the 8-7 band which are very strongly absorbed by overlapping water vapor transitions ⁽⁵⁾ and thus do not propagate through the atmosphere. Oscillation occurred on approximately six P branch transitions P(9) - P(15) within the ten vibrational bands $V^1 \rightarrow V$ $14 \rightarrow 13$ to $5 \rightarrow 4$. The calculated frequencies listed in Table 1 correspond to those transitions which were identified to within the precision of the experimental measurements corrected to vacuum.

The small signal gain measurements were made by monitoring the probe laser intensity with a Au-Ge detector after propagation through the discharge. The temporal variation of the detector signal during and after

TABLE I
SPECTRAL OUTPUT OF THE PROBE LASER AND CALCULATED
FREQUENCIES OF THE LASING TRANSITIONS

Transition		Calculated Frequency cm ⁻¹	Transition		Calculated Frequency cm ⁻¹
l V-V	P(J)		l V-V	P(J)	
5→4	11	1995 · 1050	8→7	10	1921 · 8026
	12	1991 · 0248		12	1913 · 8858
	13	1986 · 9113		14	1905 · 8361
	14	1982 · 7648	9→8	10	1896 · 1693
6→5	9	1977 · 2738		11	1892 · 2626
	10	1973 · 2955		12	1888 · 3225
	11	1969 · 2837		13	1884 · 3493
	12	1965 · 2386		14	1880 · 3429
	13	1961 · 1602		15	1876 · 3036
	14	1957 · 0486	10→9	10	1870 · 6134
7→6	9	1951 · 4551		11	1866 · 7417
	10	1947 · 5119		12	1862 · 8367
	11	1943 · 5352		13	1858 · 8984
	12	1939 · 5250		14	1854 · 9271
	13	1935 · 4817		15	1850 · 9229
	14	1931 · 4052			
	15	1927 · 2958			

TABLE i (Cont)

Transition		Calculated Frequency cm ⁻¹
¹ V-V	P(J)	
11→10	8	1852 . 7090
	9	1848 . 9395
	10	1845 . 1363
	11	1841 . 2997
	12	1837 . 4297
	13	1833 . 5265
12→11	8	1827 . 2422
	9	1823 . 5077
	10	1819 . 7396
	11	1815 . 9379
	12	1812 . 1029
	13	1808 . 2347
	14	1804 . 3335
	15	1800 . 3993
13→12	9	1798 . 1574
	10	1794 . 4242
	11	1790 . 6576
	12	1786 . 8576
	13	1783 . 0244

the discharge pulse was recorded by photographing the detector waveform displayed upon an oscilloscope and terminated by a 1 K Ω resistor.

D. RESULTS

The small signal gain g_0 is defined by the expression, $I/I_0 = \exp(g_0 l)$ where l is the active length of the discharge and I_0 and I are the probe laser beam intensities prior to and after propagation through the discharge. Gain profiles as a function of the lower rotational level $P(J)$ for various vibrational bands are shown in Figure 2. Maximum gain of approximately 4 1/2 %/cm was measured on the $6P(10)$ and $8P(10)$ transitions. Confirmation of this value was obtained by noticing that threshold lasing occurred by reflection off the cavity windows when they were normal to the optical axis. Calculations showed that the cavity loss of this configuration was approximately 4 1/2 %/cm. At threshold, this value is by definition equal to the gain. During the gain measurements, the windows were tilted to prevent oscillation.

Most of the data points within a particular vibrational band showed a smoothly varying peaked distribution as shown in Figure 2. The $5P(12)$, $5P(13)$, $6P(10)$ and $7P(10)$ transitions did not conform to this pattern and exhibited anomalously low gain. The displacements of the $6P(10)$ and $7P(10)$ data points from their corresponding smooth curves are indicated on Figure 2 by the vertical arrows.

Lacina and McAllister⁽²⁾ have attributed the absence of certain lasing transitions to resonance absorption of these lines by overlapping transitions. The extent of the overlap and the population distribution determines the degree of absorption. The $6P(10)$ transition is overlapped by the $8R(3)$ line. The separation of the unshifted lines is 0.11 cm^{-1} ,

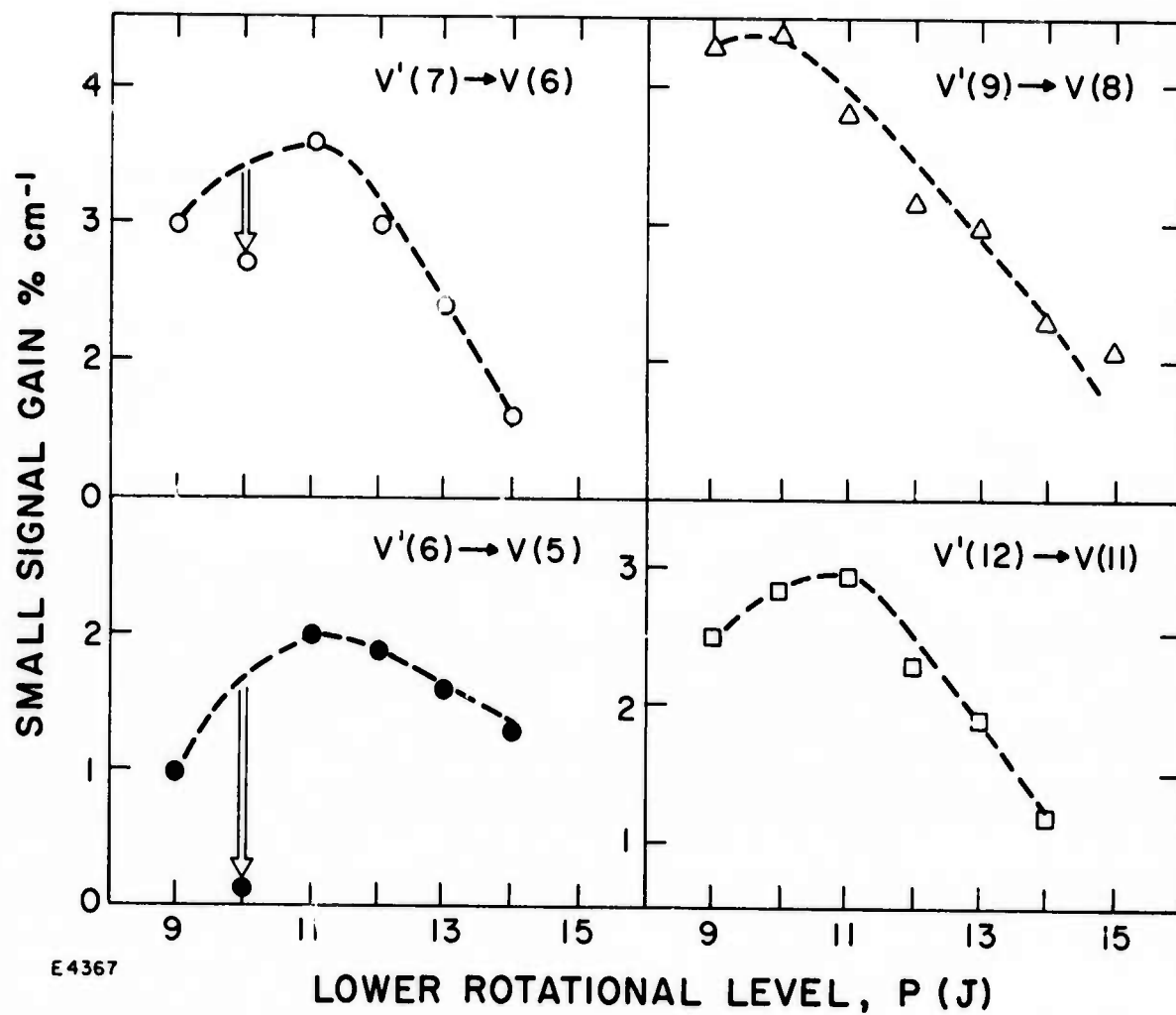


Figure 2 Measurements of Maximum Small Signal Gain as Functions of Terminal Rotational Level for Various P Branch Vibrational Transitions

and for the present experimental conditions the lines are dominated by pressure broadening with a half-width 0.03 cm^{-1} (FWHM). Thus, absorption occurs due to overlap between the wing of the 8R(3) transition and line center of the 6P(10) line. Additional overlaps exist with other levels⁽²⁾ which are not expected to be appreciably populated. The peak of the rotational distribution is expected to occur close to $J=7$; therefore, absorption will mainly occur into lower rotational levels. The coincidence for the 5P(10) transition which occurs with the 8R(7) line is even closer, to within approximately 0.03 cm^{-1} . This very close coincidence is reflected in the absence of gain. The line exhibits rapid total absorption of the probe signal.

Additional support for the hypothesis of resonance absorption by overlapping transitions was derived from small signal gain measurements on the 5P(13) transition as a function of E/N . Figure 3 shows four oscillograms of the temporal gain behaviour for the 5P(13) line for different values of E/N . Notice that for the highest E/N the line exhibits rapid total absorption and that as the E/N is reduced the absorption becomes less rapid and is preceded by gain. Eventually the probe signal is incompletely absorbed. The electron excitation cross sections shift towards higher energies for higher lying vibrational levels. Consequently reducing E/N decreases the population of the higher levels proportionality more than the lower levels. Calculations show that energy transfer by V-V collisions as E/N is reduced produces similar consequences. Therefore, as E/N is reduced these mechanisms deplete the population of the 8R(7) level correspondingly more than the 5P(13) level which reduces the extent of the resonance absorption as shown in Figure 3.

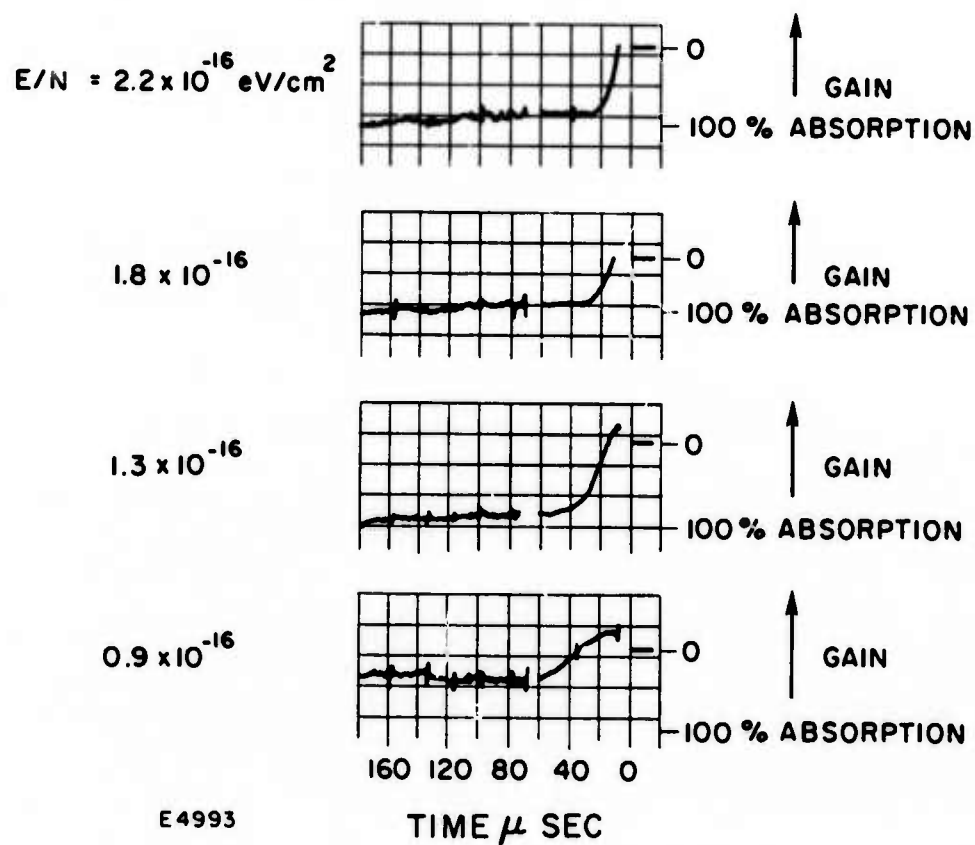


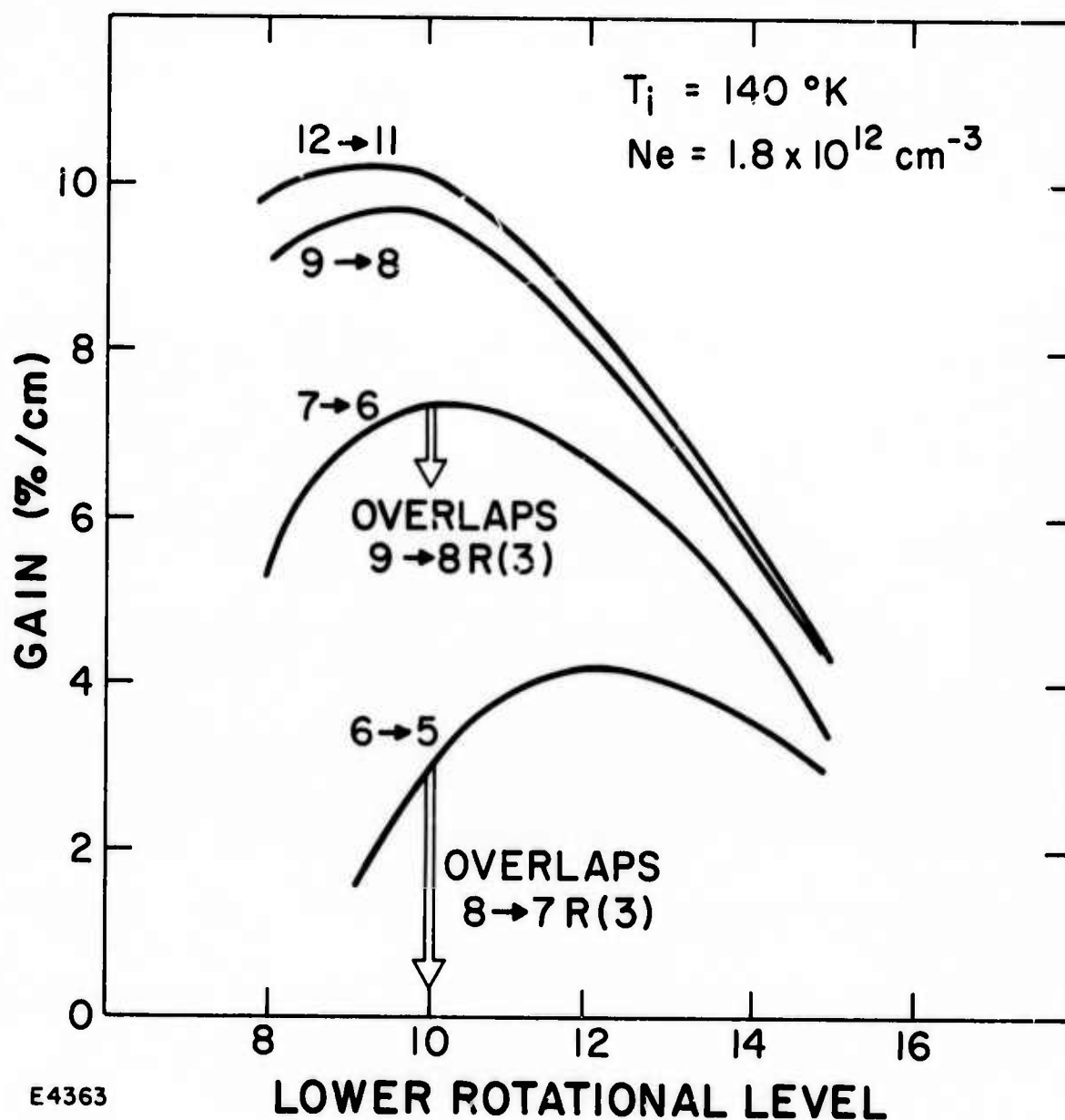
Figure 3 Temporal Variation of the Probe Laser Intensity Operating on the 5P (13) Transition for Different Values of E/N

Details of the modelling calculations have been given elsewhere. (1, 6) Figure 4 shows the predicted dependence of small signal gain on vibrational band as a function of $P(J)$ for our estimated experimental conditions. In contrast to the measurements maximum gain is predicted to occur on the $12P(10)$ transition and the magnitudes of the peak gain on all transitions are calculated to be somewhat higher than the measured values.

Gain saturation by the probe laser beam was considered but rejected as a mechanism offering a possible explanation for the disagreement between the measured and calculated values of maximum gain. Power output measurements on the 20 liter laser set a lower limit for the saturated flux intensity of approximately 10^4 watts/cm². After amplification by the medium, the probe beam intensity falls three orders of magnitude below this value. The lack of agreement probably reflects uncertainties in estimating the discharge and medium properties which are known from previous current density and interferometric measurements to show considerable lack of uniformity. (7)

Resonance absorption of the $6P(10)$ and $7P(10)$ transitions by the $8R(3)$ and $9R(3)$ levels respectively was included in the gain calculations. The effect is indicated in Figure 4 by the vertical arrows which indicate the extent of the gain suppression. The predictions are in good agreement with the measurements shown in Figure 2.

Figure 5 shows predictions of the temporal variation of small signal gain on the $P(12)$ transition for various vibrational bands. The discharge parameters are chosen appropriately to describe the estimated experimental conditions and are indicated on the figure. Each transition shows absorption initially followed by gain. This is consistent with the physical model envisaged of energy being sequentially transferred from



E4363

Figure 4 Predictions of Maximum Small Signal Gain for Various P Branch Transitions. The arrows indicate the extent of gain suppression on the 6P (10) and 7P (10) transitions when resonance absorption is included in the calculation.

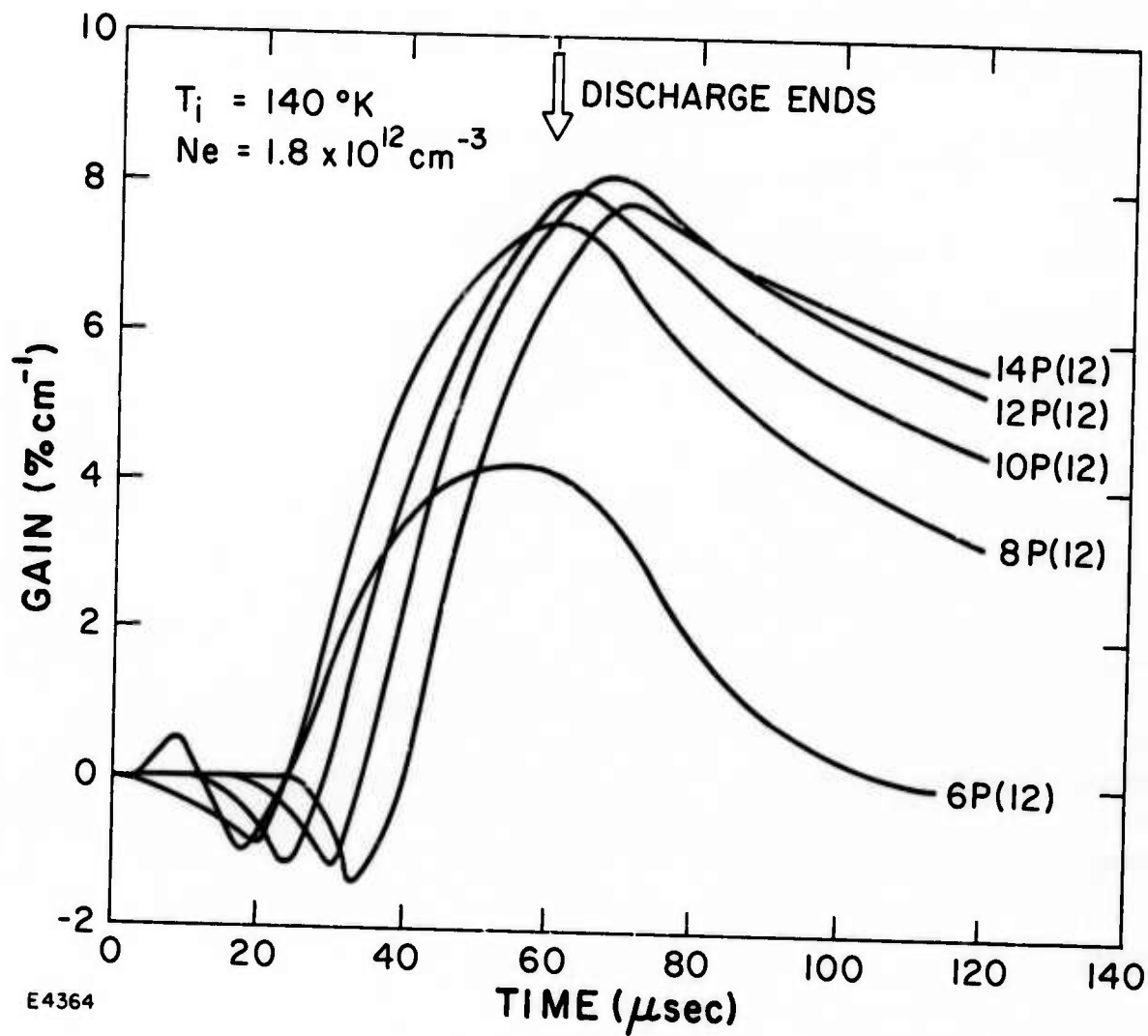


Figure 5 Predictions of the Temporal Variation of Small Signal Gain for the P (12) Line of Various Vibrational Bands

level-to-level up the vibrational ladder by V-V relaxation collisions⁽⁸⁻¹⁰⁾ which at early times establish absorption and at later times produce partial inversions and hence gain. The small gain peak predicted initially for the 6P(12) transition is associated with direct electron pumping of the $v=6$ level. Direct excitation is far less significant for the higher lying levels.^(11, 12)

For comparison with the calculations, two measurements of the temporal gain behavior together with the discharge current waveform are shown in Figure 6. The 9P(9) oscillogram is representative of all except the resonantly absorbed levels which are characterized by the behavior shown in the 6P(10) oscillogram. The majority of transitions do not exhibit the initial absorption predicted and shown in Figure 5. (The anomalous transitions exhibit initial absorption followed by either anomalously low gain or further absorption at later times in contrast to the majority of transitions which exhibit gain initially which decays at later times to zero or occasionally to absorption.) The characteristic trends of the temporal gain behavior exhibited in Figure 5 such as the times to reach threshold and peak gain as a function of vibrational level were qualitatively confirmed. Figure 7 shows the experimental and predicted times to reach threshold gain as a function of upper vibrational level for the P(12) transition. Higher lying vibrational levels require longer times to reach threshold gain lending additional support to the energy transfer mechanism proposed for establishing partial inversions.

In view of the discrepancy between theory and experiment regarding initial absorption, measurements were performed which confirmed that the detector response was sufficiently fast to respond to the predicted initial absorption. Furthermore, the signal-to-noise sensitivity was sufficient to reveal absorption levels as low as 0.2%/cm, well below the predicted

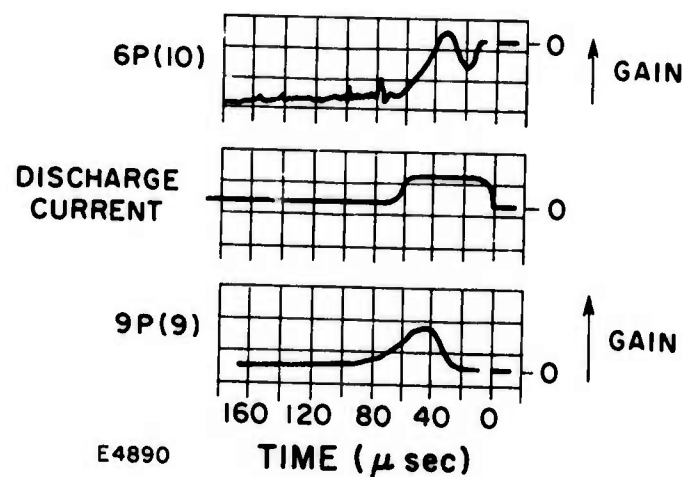


Figure 6 Temporal Variation of the Probe Laser Intensity while Oscillating on the 6P (10) and 9P (9) Transitions. The discharge current pulse is shown at the center of the figure.

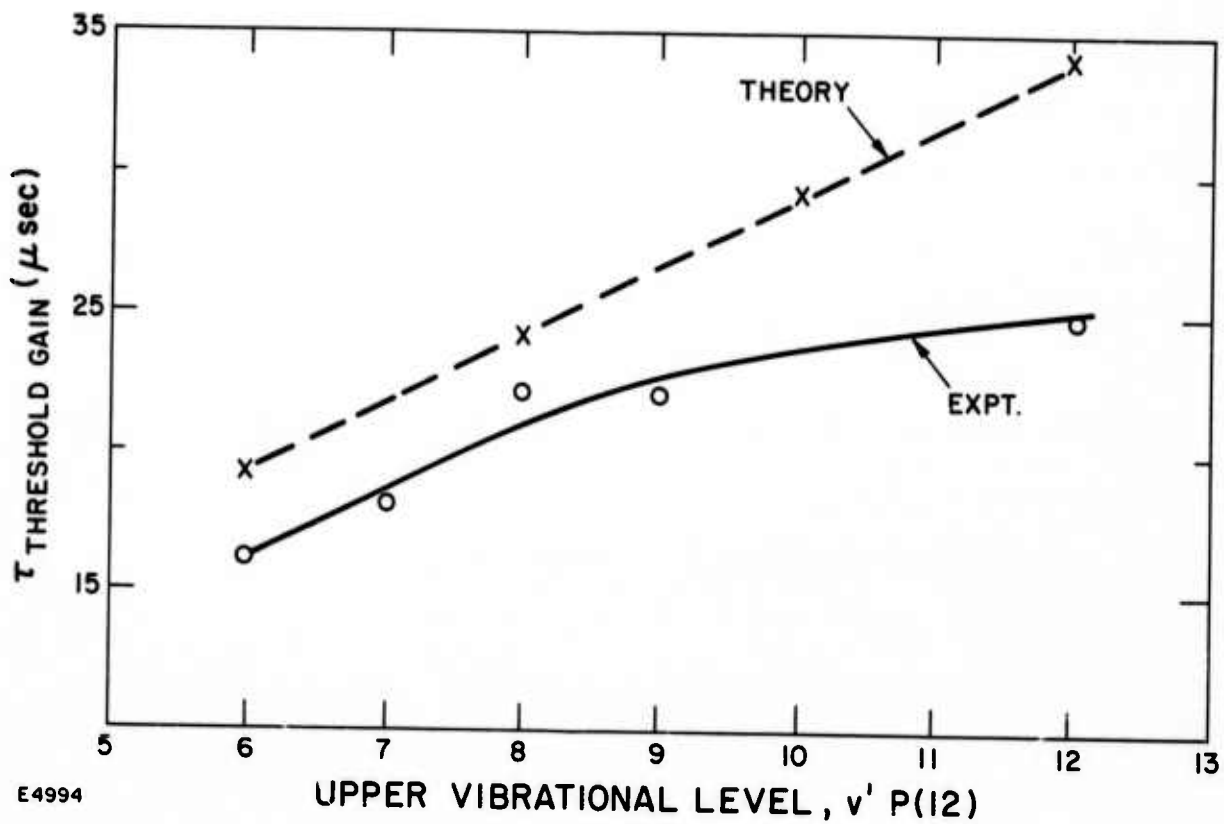


Figure 7 Theoretical and Experimental Values of the Time to Reach Threshold Gain as Functions of the Upper Vibrational Level P (12) Transition

values. Using the predicted population distributions, calculations also confirmed that saturated absorption by the medium was not responsible for the discrepancy. Additionally, further kinetics calculations were performed substituting variously increased relaxation rates for both the near and non-resonant collisions. This procedure reduced the amplitude of the predicted absorption but never suppressed it entirely. However, there is no justification for this procedure since the rates originally employed⁽¹⁰⁾ agree well with the limited available experimental data.⁽¹³⁾ Thus; this disagreement between measurement and calculation with regard to initial absorption is not understood.

The previous measurements were performed along the center line of the discharge volume. In order to investigate the effect of inhomogeneities in the electrical discharge and the gas density the probe laser beam was translated 10 cm to the edge of the anode-cathode region while remaining midway between them. Similar gain measurements showed that the character of the temporal variation remained generally unchanged but did reveal reduced gain of approximately 25% on those lines investigated.

In conclusion, the measurements show good qualitative agreement with the kinetics calculations except for the unexplained absence of absorption preceding gain. Differences between the measured and calculated magnitudes and location of peak gain may be accounted for by uncertainties associated with inhomogeneities in the electrical discharge and gas density. The measurements support the suggestion that resonance self-absorption exists on a number of transitions and calculations which include this effect compare well with the experimental data. It is recognized that this mechanism will play an important role in determining the atmospheric transmission properties of the high pressure carbon monoxide electric discharge laser.

III. UNSTABLE RESONATOR

An unstable resonator configuration has been designed and constructed for use in conjunction with the water vapor absorption cell for selected line operation of the 20 liter laser. The large uniformly filled mode volume offered by the unstable resonator makes it a suitable choice for such an application.

Power measurements and burn patterns have been made. The latter indicates a nonuniform intensity distribution which is ascribed to medium inhomogeneities. The design consisted of a single-ended confocal configuration employing a square convex output coupling mirror and a larger diameter concave mirror. The square output coupling mirror offers a more uniform intensity distribution in the lowest-loss mode and better mode discrimination than a circular mirror.

The approximate size of the square output mirror was determined by the area of the laser medium which was to be utilized (approximately 5x5 cm) divided by the magnification of the system. The exact size of the output coupling mirror was arrived at by requiring that the equivalent Fresnel number of the system be half integral. The equivalent Fresnel number F_E is defined by

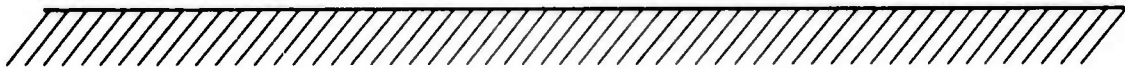
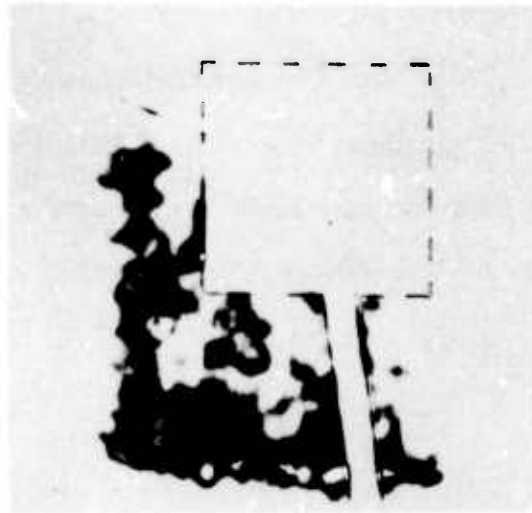
$$F_E = \frac{a^2}{4\lambda L} \left(1 - \frac{L}{R}\right)$$

where a is the radius and R the radius of curvature of the mirror, L the mirror separation and λ the wavelength. The purpose of this constraint is to optimize transverse mode discrimination.

It is generally desirable to make the magnification of such a system as large as possible in order to minimize the obscuration due to the output coupling mirror. However, if it is made too large, there will be insufficient feedback to sustain lasing action. For this application, the coupling was chosen to be 50% which corresponds to a magnification of $\sqrt{2}$. These considerations determined the size of the output coupling mirror to be 3.3 cm square. The separation of the mirrors determined by the size of the laser and the water vapor cell was 14-1/2 feet. The radius of the output coupling mirror was 75 feet and the larger concave mirror 100 feet. The tolerances imposed on the figures of the mirrors were chosen on the basis of the "small reduction of center field intensity criterion." This required that the figures be accurate to $\frac{\lambda}{16}$. The two elements were arranged on the center line of the discharge and carefully aligned with an autocollimator.

A photograph of the near field burn pattern obtained is shown in Figure 8, the location of the anode and cathode are indicated. Also visible in the photograph is the outline of the square output coupling mirror and in the lower portion one of the arms of the spider mount support. The highest intensity occurs near the lower portion of the pattern which is closest to the cathode. Similar measurements by Northrop yielded quite different results with areas of highest intensity being nearer to the anode. The lack of uniformity in their case was interpreted in terms of electron scattering which reduced the relative electron density near the anode thereby increasing the medium resistivity and hence the energy deposition. In the present system this effect is also expected to occur but the intensity distribution is believed to be dominated by the density variation within the

ANODE



CATHODE



E-BEAM

E 5027

Figure 8 The Near Field Burn Pattern Obtained Using the Unstable Resonator Configuration

medium. Previous interferometric measurements of medium homogeneity revealed considerable density gradients. The cryogenic gas entering through the porous cathode is heated through conduction and radiation as it traverses the cathode-anode gap. However, since the anode is cooled by circulating LN_2 the temperature of the gas in the vicinity of the anode is reduced which imposes a reverse temperature gradient. The net effect is to relatively reduce the E/N in the upper discharge region towards the anode thus reducing the energy deposition and producing the nonuniform pattern shown in the figure. The lateral displacement of the pattern is believed to be associated with misalignment of the unstable resonator optics.

IV. WATER VAPOR ABSORPTION CELL

The water vapor absorption cell is to be used in conjunction with the unstable resonator in an intracavity configuration. The purpose is to pursue studies of selected-line operation. A schematic of the absorption cell and the associated equipment is shown in Figure 9. The construction is of stainless steel except for the oven enclosure which is thin-walled aluminum.

The oven enclosure, transfer line and water reservoir are wrapped with heater tapes, with a number of independent temperature controllers. Temperature monitoring is provided by ten thermocouples placed at various points over the system. The pressure within the cell is measured with a high temperature differential pressure transducer. Additive gases may be introduced to the cell via the metering valve. The assembly is pumped by a 3 cfm mechanical pump which permits a base pressure of approximately 10μ to be achieved. A liquid nitrogen cold trap permits the water vapor to be trapped whenever it is necessary to evacuate the system. The clear aperture of the cell is $5\frac{1}{2}$ " in diameter, it is limited to $3\frac{1}{2}$ " by the two cylinders at either end of the oven enclosure. The purpose of the cylinders is to reduce convective air circulation around the windows. The optical length of the cell is 20". The cell windows are of calcium fluoride and 6" in diameter they are placed at normal incidence to the optical axis and have been anti-reflecting coated at 5μ .

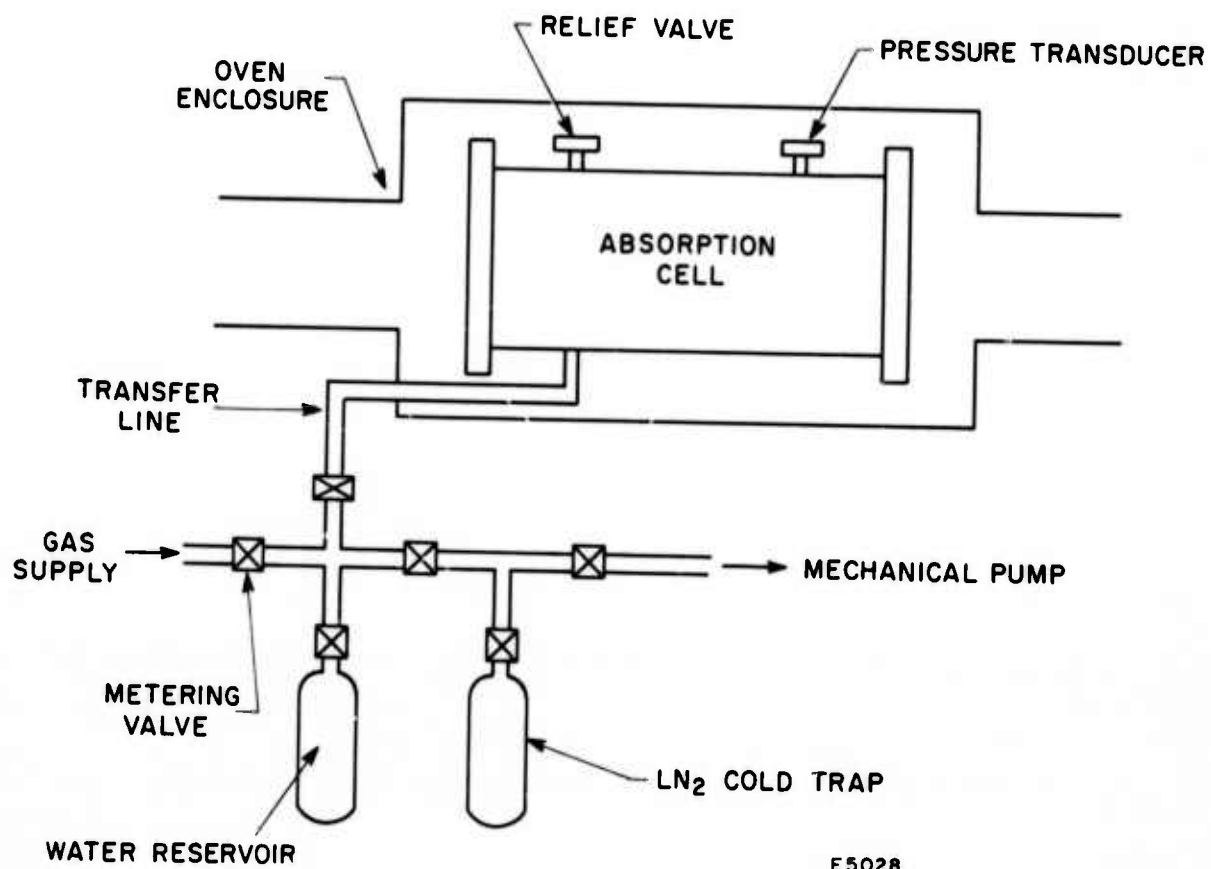


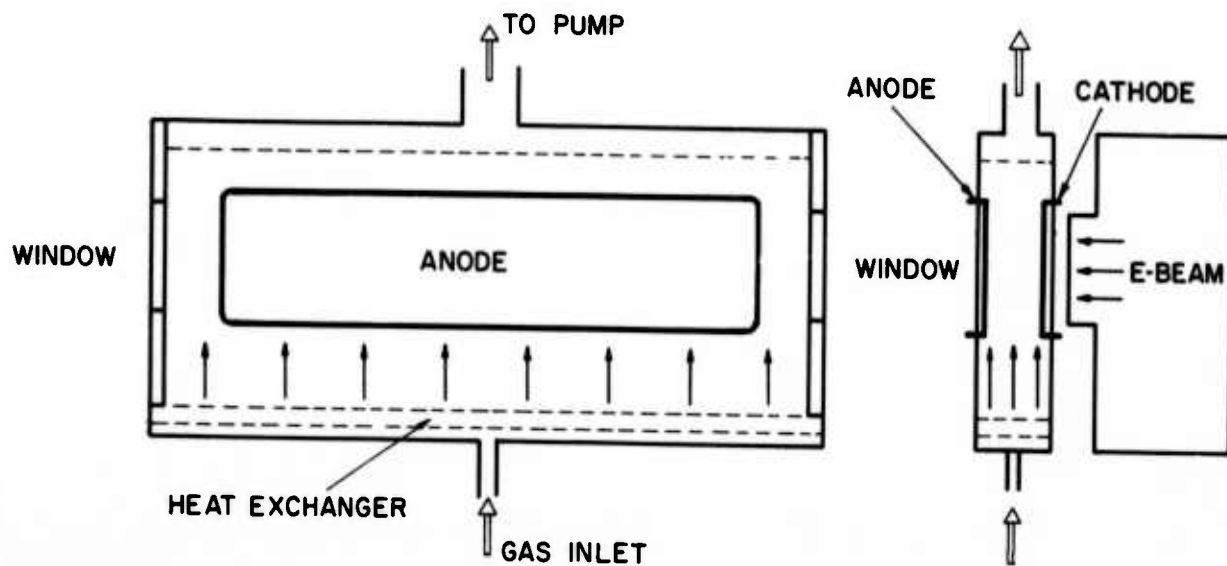
Figure 9 Schematic of the Water Vapor Absorption Cell

Prior to installing the cell inside the unstable resonator cavity interferometric measurements will be performed to check the medium quality inside the absorption cell.

V. NEW DISCHARGE CAVITY/FLOW SYSTEM

A new transverse gas flow system has been designed and constructed in this continuing program to overcome the thermal nonuniformities observed in the original discharge cavity. A schematic on the flow system is shown in Figure 10. The basic concept of the new system is to introduce the gas through a heat exchanger and allow free convection boundary layers to be established on the room temperature side and end walls. The flow direction is vertically upwards to ensure that buoyancy effects are favorable and to avoid recirculation zones. The transverse flow configuration in this new cavity design has the advantage of utilizing the smallest cross sectional area in the system resulting in maximum flow velocity for a given pumping speed.

The new cavity flow system is designed for operation over the temperature range from 80°K to 300°K and the pressure up to 1 atm. The overall design goal is to obtain the beam quality that is 1.5 times diffraction-limited or better. This corresponds to a maximum of a $1/10$ fringe variation across the cavity. A new flow system is designed to be compatible with the existing 20 cm x 100 cm electron gun and to operate with a maximum discharge width of the order of 10 cm. The system is designed to operate initially with a transverse flow velocity of 100 cm per second and a corresponding mass flow of the order of 150 grams per second. Provision has been made for increasing the transverse flow velocity up to 1000 cm per sec should this prove necessary.



D9069

Figure 10 Schematic of Transverse Flow/Discharge Cavity System

The design concept of the heat exchanger was to use a pre-cooled porous plug with sufficient thermal capacity to cool the gas for transient operation of approximately 10 sec. This is more than sufficient for pulsed operation and avoids the necessity for construction of a massive heat exchanger with all its associated liquid nitrogen plumbing.

A. BOUNDARY LAYER CALCULATIONS

Medium homogeneity requirements for a diffraction-limited output beam place stringent limits on the allowable variations in optical path length in the cavity. Since the cavity walls are warmer than the gas, buoyancy effects appear along with forced convection. In addition, a uniform flow in velocity entering the cavity is required to allow the formation of boundary layers on the windows. Boundary layers (as opposed to recirculation zones) are desirable because they concentrate the density change into a narrow distance, leading to a low path length variation relative to a uniform medium. A configuration such as shown in Figure 10 is clearly suitable for this purpose.

The maximum variation in the quantity $\Delta\ell$, where

$$\Delta\ell = \int_0^{\ell} \frac{\rho - \rho_{\infty}}{\rho_{\infty}} dy \quad (1)$$

between any two paths will be set here at 1/10 of a fringe corresponding to a 1.5 times diffraction limited central spot. In the above, ρ is local density, ρ_{∞} is the bulk flow mean density, ℓ is the cavity length, and y is distance perpendicular to the windows in the lasing direction. At 5μ , with 1/2 amagat density, the value of $\Delta\ell$ for 1/10 fringe is 3 mm. The boundary layer calculations given below, indicate that this constraint can be readily satisfied.

There are three dimensionless parameters of interest. The first one is the Reynolds number, $Re_d = ud/\nu$, where u is the bulk flow velocity, d is the cavity width, and ν is the kinematic viscosity of the gas. The Reynolds number is the parameter associated with forced convection. For $u = 10^2$ cm/sec (a lower bound) $d = 10$ cm, $\nu = 0.2$ cm²/sec, $Re_d = 5 \times 10^3$. Free (buoyancy-driven) convection is controlled by the Grashof number $Gr_d = g\beta \theta_w d^3/\nu^2$, where g is the acceleration of gravity, β is the compressibility of the gas and θ_w is the temperature difference between the window and the bulk flow. With $\theta_w = 200^\circ\text{K}$ (bulk flow at 100°K), and an effective $\beta = \frac{1}{T^*}$ where $T^* = 200^\circ\text{K}$, $Gr_d = 2.5 \times 10^7$.

The parameter that controls the relative importance of forced convection and buoyancy is the Froude number $Fr_d = u/(g\beta \theta_w d)^{1/2}$. The Froude number is simply the ratio $Re_d/Gr_d^{1/2}$. In our case, $Fr_d \geq 1$. Buoyancy is, therefore, not a small perturbation on forced convection, but rather of equal importance. Because of this, it is essential to use the optimum flow configuration of Figure 1 for which the buoyancy forces are in the flow direction.

The Reynolds and Grashof number can be written in terms of distance along the wall (x) to determine whether the boundary layer will be laminar or turbulent, at $x = 40$ cm, $Re_x = 2 \times 10^4$ and $Gr_x = 1.6 \times 10^9$. A pure forced laminar boundary layer will undergo transition to turbulence at $Re_x \sim 10^5$, whereas a free layer will do so at $Gr_d \sim 10^9$. There is a possibility, then, that the boundary layer on the window may be turbulent.

The change in optical path length Δl in the boundary layer is obtained by integration of Eq. (1) from 0 to δ , where δ is the boundary layer

thickness. The change in path length which is caused by turbulent fluctuations in the boundary layer is much smaller than Δl in Eq. (1), and will be ignored. If Δl did not vary from point to point (in the stream-wise direction) in the boundary layer, each ray would travel the same path length. It is the change in Δl from point to point as the boundary layer becomes thicker that affects the medium homogeneity.

The problem, then is the computation Δl as a function of stream-wise location for a boundary layer on a vertical heated wall where both forced and free convection are present. The structure of the laminar layer has been obtained analytically and numerically by several authors. (14 - 18) In this report an approximate solution is obtained for the first order perturbation on the asymptotic solutions for pure forced convection and pure free convection using an integral formulation for the turbulent boundary layer equations. Characteristic length scales for optical path variations will be presented.

1. Forced Convection Asymptotic Case

In the absence of pressure gradients and body forces the boundary layer momentum equation for the pure forced convection case is⁽¹⁹⁾

$$\rho \int_0^{\delta_1} u (u_\infty - u) dy = \tau_w \quad (2)$$

where δ_1 is the pure forced convection boundary layer thickness, u is velocity, u_∞ is velocity far away from the wall, and τ_w is wall shear stress.

Assuming

$$u = u_{\infty} \left(\frac{y}{\delta_1} \right)^{1/7}$$

$$\tau_w = 0.0228 \rho u_{\infty}^2 \left(\frac{\nu}{u_{\infty} \delta_1} \right)^{1/4} \quad (3)$$

the well known result for δ_1 is obtained,

$$\delta_1 = 0.376 \left(\frac{\nu}{u_{\infty}} \right)^{1/5} x^{4/5} = \frac{0.376 x}{(Re_x)^{1/5}} \quad (4)$$

where ν is the kinematic viscosity, x is distance along the window, and Re_x is Reynolds number, $Re_x = u_{\infty} x / \nu$.

If the boundary layer is heated in a gravity field, buoyancy forces arise. If the buoyancy force is included in the momentum equation using the approximation $\Delta\rho/\rho = (T - T_{\infty})/T_{\infty}$, Eq. (2) becomes

$$\rho \int_0^{\delta_1 + \delta_1'} u (u_{\infty} - u) dy = \tau_w - \frac{\rho g}{T_{\infty}} \int_0^{\delta_1 + \delta_1'} \Theta dy \quad (5)$$

where g is the acceleration of gravity, T_{∞} is the gas temperature far away from the wall, $\Theta = T - T_{\infty}$, and δ_1' is the perturbation in boundary layer thickness caused by the addition of buoyancy.

$$\Theta = \Theta_w \left[1 - \left(\frac{y}{\delta} \right)^{1/7} \right] \quad (6)$$

(where Θ_w is $T_{\text{wall}} - T_{\infty}$). We will also assume that the buoyancy force is small, and that $\delta_1' \ll \delta_1$. It is possible to derive equations for parameters describing the perturbations in boundary layer velocity and temperature from the momentum and energy equations taking constant δ_1 . This

procedure requires that one choose suitable profiles for the perturbations. Since there is no information available on such profiles, any profile choice would necessarily be arbitrary. For this reason, we will assume that buoyancy appears as a change δ_1' in the boundary layer thickness with the unperturbed velocity profile (Eq. (3)). Then we can obtain an equation for the perturbation in δ_1 caused by buoyancy by use of Eqs. (2) - (6) and this leads to the result

$$\delta_1' \approx -0.241 \left(\frac{\nu}{u_\infty} \right)^{1/5} \frac{g(\Theta_w/T_\infty)}{u_\infty^2} x^{9/5} \quad (7)$$

Buoyancy thus reduces the boundary layer thickness at a given value of x , since the perturbed thickness is $(\delta_1 + \delta_1')$.

2. Free-Convection Asymptotic Case

Eckert and Jackson⁽²⁰⁾ have solved the problem of pure free-convection turbulent boundary layer. Taking integral equations for momentum and energy, assuming $Pr = 1$, and using

$$u = u_2 \left(\frac{y}{\delta} \right)^{1/7} \left(1 - \frac{y}{\delta} \right)^4 \quad (8)$$

$$\Theta = \Theta_w \left[1 - \left(\frac{y}{\delta} \right)^{1/7} \right] \quad (9)$$

one can obtain

$$\delta_2 = 0.595 (Gr_x)^{-1/10} x \quad (10)$$

where δ_2 is the free convection layer thickness and Gr_x is the Grashof number, $Gr_x = g(\Theta_w/T_\infty) x^3/\nu^2$. For comparison, in the laminar case $\delta_2 \sim x^{1/4}$ instead of $\delta_2 \sim x^{7/10}$ as in Eq. (10).

Introducing a perturbation consisting of an external flow (velocity u_∞) into the integral energy equation, we obtain

$$\rho C_p \frac{d}{dx} \int_0^{\delta_2 + \delta_2'} (u + u_\infty) \Theta dy = q_w \quad (11)$$

Proceeding as before, we obtain an equation for the perturbation, δ_2' , in δ_2 caused by the external flow. This leads to the solution

$$\delta_2' \approx -0.910 \frac{u_\infty}{v} \left(\frac{g(\Theta_w/T_\infty)}{v^2} \right)^{-6/10} x^{2/10} \quad (12)$$

The external flow reduce δ_2 at a given x , since the perturbed thickness is $(\delta_2 + \delta_2')$.

3. Results for Optical Path

The results obtained above for the perturbed boundary layer thickness can now be used to calculate optical path lengths through the boundary layer.

With the approximation $(\rho - \rho_\infty)/\rho_\infty = \Theta/T_\infty$, Eq. (1) becomes

$$\Delta l = \int_0^\delta \frac{\Theta}{T_\infty} dy \quad (13)$$

Using Eqs. (4), (6), (7) and (13), we obtain for the forced-convection asymptotic case

$$\Delta l_1 \approx 0.047 \frac{\Theta_w}{T_\infty} x Re_x^{-1/5} \left(1 - 0.64 \frac{Gr_x}{Re_x^2} \right) \quad (14a)$$

Similarly, using Eqs. (9), (10) and (12)

$$\Delta l_2 \approx 0.074 \frac{\Theta_w}{T_\infty} x Gr_x^{-1/10} \left(1 - 1.53 \frac{Re_x}{Gr_x^{1/2}} \right) \quad (15a)$$

The dominant parameter in this problem is a Froude number based on x , where

$$Fr_x = \frac{u_\infty}{[g (\Theta_w/T_\infty) x]^{1/2}} = \frac{Re_x}{(Gr_x)^{1/2}} \quad (16)$$

There is then a scale length L^* for distance along the window,

$$L^* = \frac{u_\infty^2}{g (\Theta_w/T_\infty)} \quad (17)$$

If $x \ll L^*$, forced convection is dominant. As x becomes very large ($x \gg L^*$), free convection (i. e., buoyancy) dominates. Neither Eq. (14) nor Eq. (15) applies when $x/L^* \sim 1$.

In nondimensional form, the above results are

$$\Delta l_1^* \approx 0.047 x^{*4/5} (1 - 0.64 x^*) \quad (\text{Forced Convection}) \quad (14b)$$

$$\Delta l_2^* \approx 0.074 x^{*7/10} (1 - 1.53 x^{*-1/2}) \quad (\text{Free Convection}) \quad (15b)$$

Here

$$x^* = x/L^* \quad (18)$$

$$\Delta l^* = \Delta l/Y_{\text{TURB}}^* \quad (19)$$

where Y_{TURB}^* is a scaling length for the optical path variation, and is defined by

$$Y_{\text{TURB}}^* = \frac{(\Theta_w/T_\infty)^{1/5} u_\infty^{7/5} \nu^{1/5}}{g^{4/5}} \quad (20)$$

Following a procedure similar to that presented above for a laminar layer leads to a different scaling length Y_{LAM}^* ,

$$Y_{LAM}^* = \left[\frac{(\Theta_w/T_\infty) u_\infty \nu}{g} \right]^{1/2} \quad (21)$$

while L^* is as in Eq. (17). Values for L^* , Y_{TURB}^* and Y_{LAM}^* as functions of u_∞ and Θ_w/T_∞ for CO, N_2 mixtures at 1 amagat density are shown in Figure 2. Since the values of ν for CO and N_2 are nearly identical, the mixture ratio is unimportant. In Figure 11 (Θ_w/T_∞) and ν have been evaluated using a reference temperature halfway between T_w and T_∞ to replace T_∞ for large $(T_w - T_\infty)$. Regions in x , u_∞ , and T_∞ where the flow is turbulent have been delineated using the criteria $Re_x = 2 \times 10^5$ or $Gr_x = 10^9$.

Using the results of Ref. 15, Δf for a laminar layer can be obtained. Figure 12 shows a plot of Δf vs downstream distance x from the leading edge (the heat exchanger) using a reference temperature T^* of $200^\circ K$ to replace T_∞ , for conditions of interest for the CO laser, $u_\infty = 100$ cm/sec, $d = 10$ cm, and $\Theta_w = 200^\circ K$, for a CO- N_2 mixture.

Figure 13 shows Δf vs x for a turbulent boundary layer for the same operating conditions as above. Since the asymptotic expressions Eqs. (14) and (15) do not join up smoothly, and are not valid beyond the point where the perturbations are $\sim 25\%$ of the unperturbed value, lines were drawn tangent to the perturbed free and forced Δf at the point where the perturbation is 25% of the unperturbed value. These lines form the combined flow line shown in Figure 13. Lines showing the perturbed values (Eqs. (14) and (15)) are also included in Figure 13.

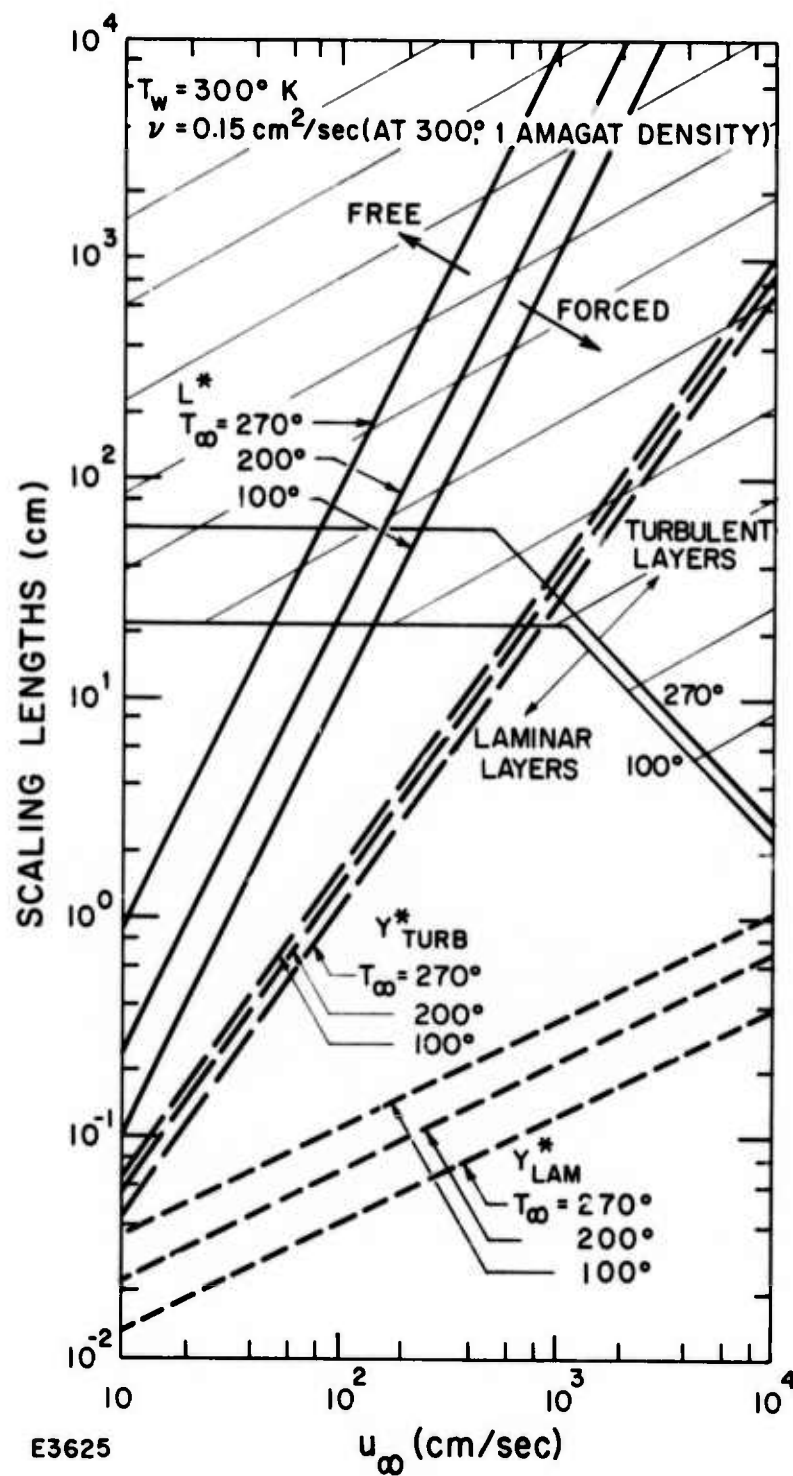


Figure 11 Scaling Lengths vs Flow Velocity, u_∞ , and the Gas Temperature T_∞ for CO-N₂ Mixtures and 300°K Wall Temperature. The free and forced convection regions are shown.

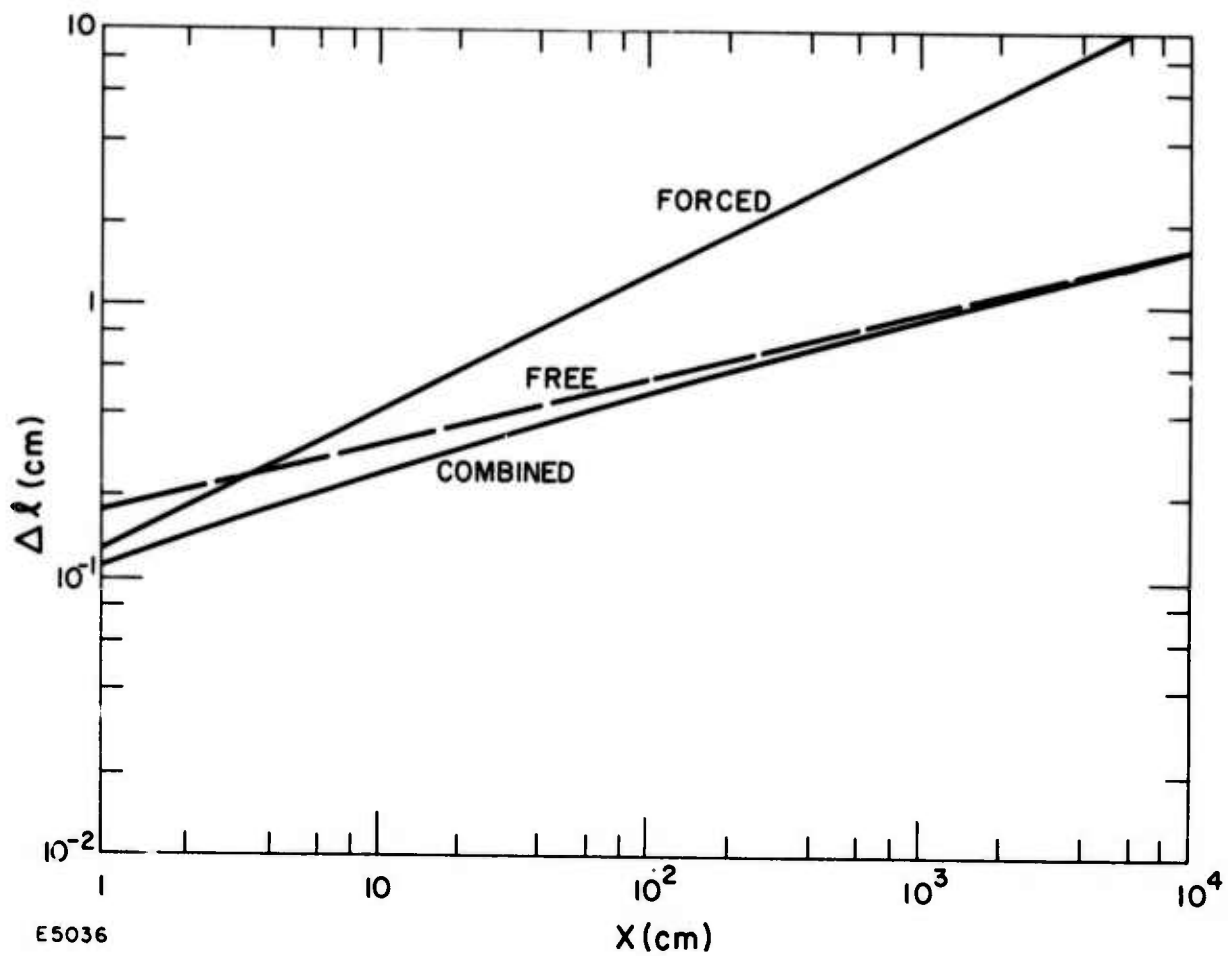


Figure 12 Laminar boundary layer results (Ref. 2) in CO-N₂ mixtures for $\Delta \ell$ vs the downstream distance from the leading edge, x . $u_\infty = 100$ cm/sec and $\Theta_w = T^* = 200^\circ\text{K}$.

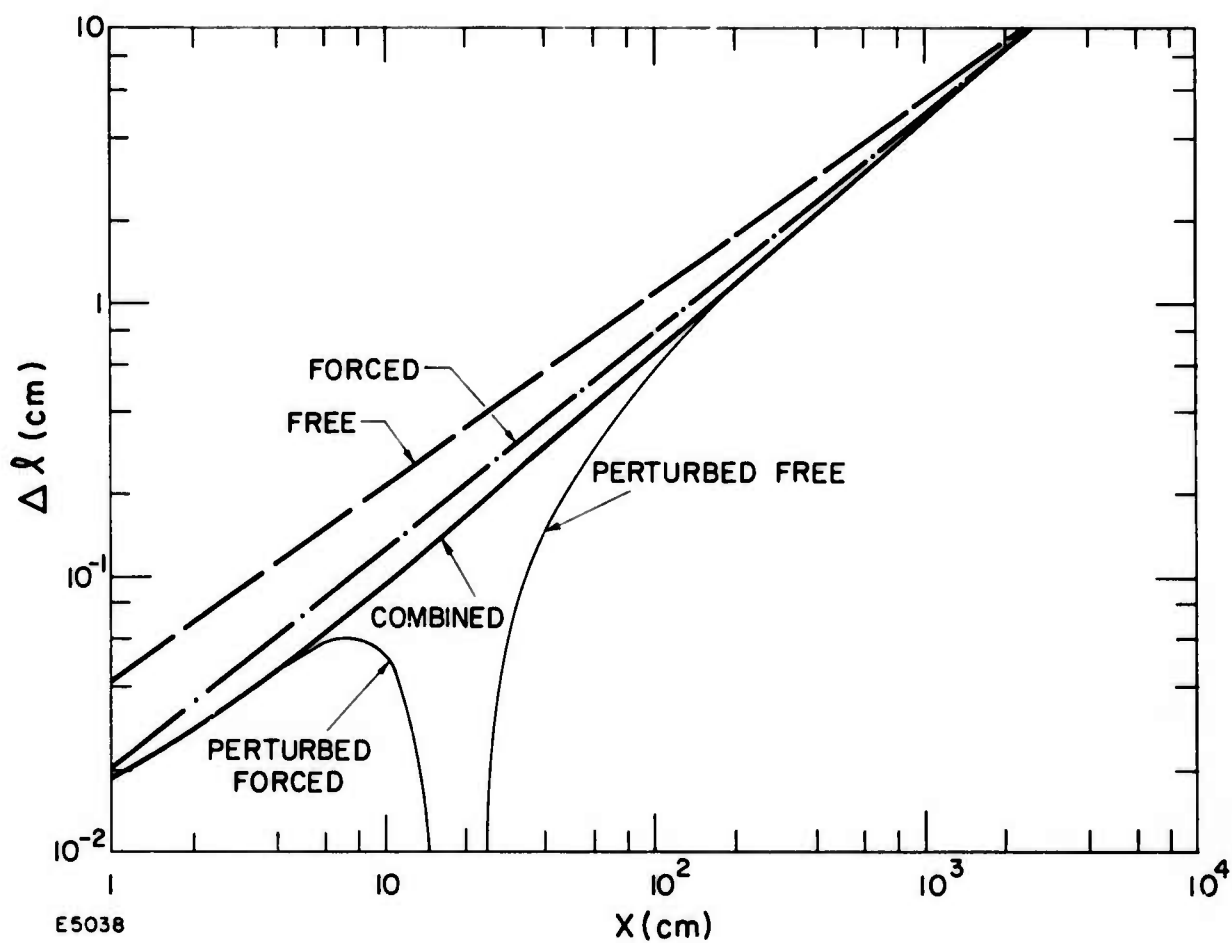


Figure 13 Turbulent boundary layer results, Eqs. (14) and (15), in CO-N₂ mixtures for $\Delta \ell$ vs the downstream distance from the leading edge, x . $u_{\infty} = 100$ cm/sec and $\Theta_w = T^* = 200^\circ\text{K}$

From Figure 12 it can be seen that if the window extends from $x = 20$ cm to $x = 40$ cm; and the flow remains laminar, the variation in $\Delta\ell$ from top to bottom will be 0.07 cm, or 1.4 mm for two windows. On the other hand, assuming that the boundary layer is laminar at $x = 20$ cm (Re_x and Gx are well below transition levels at $x = 20$ cm) and turbulent at $x = 40$ cm, from Figures 12 and 13 the variation in $\Delta\ell$ would not be any greater. Since the boundary layer is transitional, there is little difference in the thicknesses which is well within the required limit. The turbulent layer grows at a very fast pace, however, so that for larger systems, say $x = 10^2$ cm, the difference between a turbulent layer and a laminar layer would be large.

B. DESIGN OF HEAT EXCHANGER

Following some preliminary investigations it was decided to use porous sintered bronze plates for the heat exchanger. This choice was based upon the requirement of a large thermal capacity and efficient heat transfer to the gas. It should be noted that free stream temperature variations due to dynamic effects are negligible in the present case with flow velocities less than 1000 cm per sec.

The overall design of the heat exchanger is shown in the schematic of Figure 14. It consists basically of three uniform sintered bronze plates mounted in an isothermal aluminum box. A series of 1/4 inch copper tubes, spaced 2 inches apart, are embedded in the sintered bronze plates and connected via manifolds to the coolant supply, usually liquid nitrogen. The manifolds are split into two counterflow sections to reduce any transverse temperature gradients. The porosity of the plates was chosen to

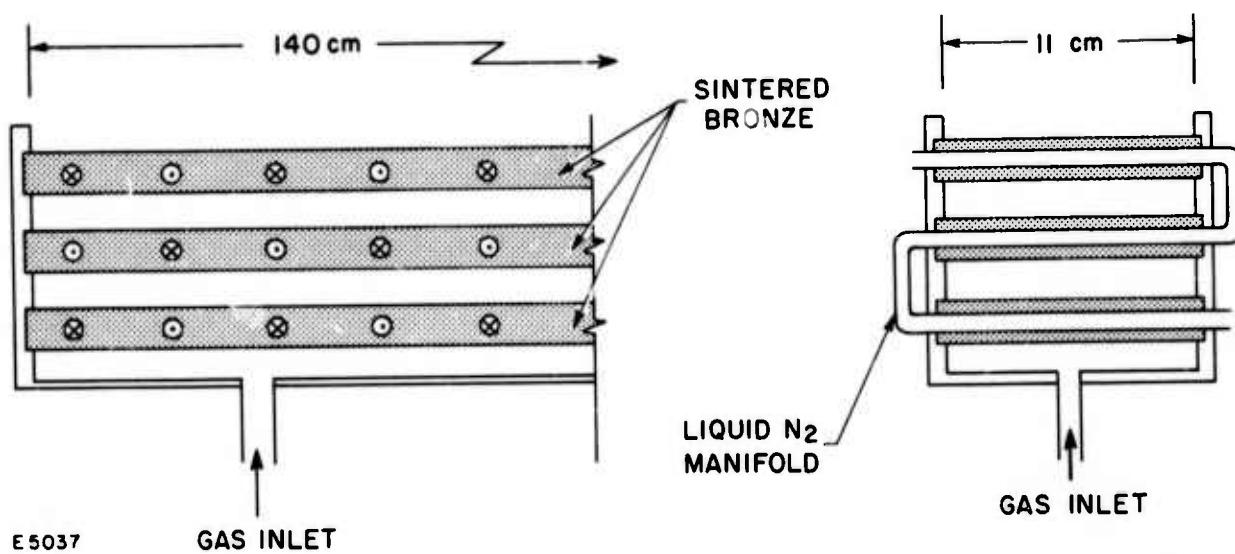


Figure 14 Schematic of the Porous Plate Heat Exchanger

provide a pressure drop of approximately 1 psi across each plate based on laboratory measurements.

It can be shown analytically that large scale inhomogeneities present in the laminar flow issuing from the porous plates decay very slowly for the Reynolds numbers of interest. Thus, it is necessary to insure that the flow leaving the porous plates has good initial temperature uniformity, a fraction of a degree, to prevent significant contribution to the quantity Δl defined in Eq. (1). Calculations were made to estimate the thermal accommodation of the gas to the porous plates to ensure that the gas leaves the heat exchanger at a uniform temperature. These calculations are outlined below.

The porous plates can be viewed as a collection of long, narrow tubes of diameter D . The heat transfer in such a tube is

$$\rho C_p u_m \Delta T = 4 q_w \frac{\Delta x}{D} = 4 \left(k \frac{\partial T}{\partial r} \right) \frac{\Delta x}{D} \quad (22)$$

where u_m is the mean flow velocity ΔT is the temperature change, Δx is distance along the tube, q_w is the heat transfer rate per unit area, and r is tube radial distance. The pressure drop has the form

$$\Delta p = 4 \tau_w \frac{\Delta x}{D} = 4 \left(\mu \frac{\partial u}{\partial r} \right) \frac{\Delta x}{D} \quad (23)$$

where τ_w is the wall shear stress. If $Pr \sim 1$, then the $T(r)/\theta_w$ and $u(r)/u_m$ should be roughly the same, so that Eqs. (22) and (23) can be combined to give

$$\frac{Pr}{\theta_w} \frac{dT}{dx} \approx \frac{1}{\rho u_m} \frac{1}{2} \frac{dp}{dx} \quad (24)$$

Since the pressure drop across the plug can be ~ 1 psi ($\sim 10^5$ dynes/cm²) and $\rho u^2 \sim 10^{-3} \times (100)^2 \sim 10$ dynes/cm², the distance for the gas to accommodate to the wall temperature would be $\sim (10/10^5) \times$ (thickness of the plug).

1. Required Plate Thickness

It will be convenient to assume that the plug is made up of a number of thin plates each of thickness L . It will also be assumed that, as shown above, the gas and metal in each plate accommodate to each other. All the plates are pre-cooled to the desired final gas temperature before flowing the lasing mixture. The flow is then turned on for a period ~ 1 -10 sec. To ensure that the gas leaves the stack with the required uniformity, the last plate must not rise in temperature more than the required uniformity level during the run.

Flowing a gas of initial temperature T_g through a thin plate (i. e., of uniform temperature) initially at T_w for a time $\Delta t = L/u$, with a final temperature of T_f , a heat balance can be written for the gas and the plate,

$$\rho_g C_g (T_g - T_f) = \rho_w C_{pw} (T_f - T_w) \quad (25)$$

In the above, ρ_g is the gas density, A is the plate area, C_g is the gas heat capacity, ρ_w is the plate density, and C_{pw} is the plate heat capacity.

Taking $(dT/dt)_{\text{plate}} = (T_f - T_w)/(L/u)$, and $\rho_w C_{pw} \gg \rho_g C_p$ a differential equation for the temperature of the first plate T_1 can be obtained from Eq. (25)

$$\frac{dT_1}{dt} \approx \frac{(T_{g_o} - T_1)}{\tau} \quad (26)$$

where $\tau = (\rho_w C_{p_w}) L / (\rho_g C_{p_g}) u$, giving

$$T_1 = T_{g_o} - (T_{g_o} - T_{w_o}) e^{-t/\tau} \quad (27)$$

where T_{g_o} , is the temperature of the gas entering the stack of plates, and T_{w_o} is the initial temperature of the stack. For the second slab, the incoming gas temperature is no longer T_{g_o} , but the gas temperature leaving the first plate, or T_1 ; thus,

$$\frac{dT_2}{dt} \approx \frac{(T_1 - T_2)}{\tau} \quad (28)$$

and so on for T_3, \dots, T_n . The mass flow through each plate, $\rho_g u A$ (where A is the plate area) is the same, and the area of each plate is the same, so that τ is the same for each plate.

It can be shown by induction that the temperature of the n -th plate T_n in the stack with time is

$$\frac{T_n - T_{g_o}}{T_{w_o} - T_{g_o}} = \sum_{m=0}^{n-1} \frac{\left[t - (n-1) \frac{L}{u} \right]^m}{m! \tau^m} e^{-\left[t - (n-1) \frac{L}{u} \right] / \tau} \quad (29)$$

With typical values ($L \sim 1$ inch = 2.5 cm, $u = 100$ cm/sec),
 $\tau \sim (5 \times 0.4) \times 2.5 \text{ cm} / (10^{-3} \times 1) \times 10^2 \text{ cm/sec} \sim 50 \text{ sec}$. Then for a
 10 - second run, with 5 plates and $T_{g_o} = 300^\circ\text{K}$, $T_{w_o} = 100^\circ\text{K}$,

$$T_5 \Big|_{t=10 \text{ sec}} = (100 + 0.06)^\circ\text{K} \quad (30)$$

Because of frictional heating in the plates, the absolute temperature of the whole stack will rise during the run. The energy deposited in the plates is $\approx \Delta p u A t$. This corresponds to a temperature rise ΔT ,

$$\Delta T \approx \frac{(\Delta p/L) ut}{\rho_w C_{p_w}} \quad (31)$$

For $\Delta p/L \sim 1$ psi/inch $\sim 2.5 \times 10^4$ dyne/cm²/cm, $\Delta T \approx 1.2^\circ\text{K}$ over a 10 sec run, or 0.12 K/sec. If the flow uniformity is 5%, then the temperature variation will be $0.1 \times 1.2 \approx 1/8^\circ\text{K}$. There is also a difference in temperature between the center of each pore and the outer part $\sim (\gamma - 1) \text{Pr} M^2/8 \sim 10^{-6}$ where M is the flow Mach number or $\Delta T \sim 10^{-6} \times 100^\circ\text{K} \sim 10^{-4}^\circ\text{K}$, which is insignificant.

In summary, if the plates are properly precooled, the gas will leave the stack with variations in temperature less than the level of $1/6^\circ\text{K}$ required for diffraction-limited operation.

C. DISCHARGE ELECTRODE CONFIGURATION

Some consideration has been given to the design to the discharge electrodes in order to minimize the nonuniformities in the deposition of electrical energy in the gas. These nonuniformities arise from scattering of the primary electrons and nonuniform transverse electric field distribution due to the finite extent of the electrodes. These in turn give rise to varying conductivity in the discharge region.

The discharge can be thought of as nonuniform, nonlinear two-dimensional resistor between the anode and cathode. Mathematically the resistor is described by Poisson's equation

$$\nabla \cdot (\sigma \nabla \phi) = 0 \quad (32)$$

$$\vec{E} = -\nabla \phi \quad (33)$$

where ϕ is the potential and \vec{E} is the electric field. Eq. (32) is nonlinear because the conductivity σ is a function of E .

Equation (32) has been studied analytically for special cases. ⁽²¹⁾

This was done by a perturbation expansion. The small parameter in the expansion was the ratio E_{\parallel}/E_{\perp} where E_{\parallel} is the electric field parallel to the anode/cathode surfaces and E_{\perp} was the electric field perpendicular to the anode/cathode surfaces. It was further assumed that the anode and cathode were planar and infinite. However, the E-beam was finite in extent. For a practical laser it was necessary to solve Eq. (32) in arbitrary geometry to allow for changes in design. Because of the complexity of the problem it is necessary to seek a numerical solution to Eq. (32). This was done by modifying JASON, ⁽²²⁾ a nonlinear electrostatic code developed by Dr. Sackett of Lawrence Berkeley Laboratory. This code has been tested to insure that it does in fact solve nonlinear problems accurately with errors in the potential and electric field of less than 0.1% and 1% respectively.

The conductivity σ is a function of the local electric field and ionization rate S by the high-energy electrons. This dependence will vary from one gas mixture to the next. No measurements of the recombination rate have been made in an 80-20 N_2 -CO mix. However, measurements ⁽²³⁾ in pure N_2 indicate that the recombination rate varies as $(T_e)^{-1.8}$. A similar dependence on the electron temperature T_e was obtained for CO. ⁽²⁴⁾ In the subsequent analysis it is assumed that the recombination rate in the mixture of interest is proportional to $(T_e)^{-1.8}$. From the AERL Boltzman code it is known that T_e in an 80-20, N_2 -CO mix is proportional to $(E)^{0.25}$ while the drift velocity $v_D \propto (E)^{0.6}$. Combining this information one can write ⁽⁸⁾

$$\sigma = C (E)^{-0.2} S^{0.5} \quad (34)$$

where C is a constant.

The ionization rate S is proportional to the energy deposition by high-energy electrons. For the conditions in the CO laser this can be written approximately as⁽²⁵⁾

$$S \approx \exp(-\gamma x) \left[\tan^{-1} \left(\frac{y+a}{x} \right) - \tan^{-1} \left(\frac{y-a}{x} \right) \right] \quad (35)$$

where $\gamma = cE/2w$ and w is the electron energy. The electron beam is assumed to have a width $2a$ located at $x = 0$ and between $-a \leq y \leq a$.

Figure 15 shows the computer plot for lines of constant potential. Note that the lines are more closely spaced at the edge of both electrodes. In these regions the electric field is about 25% larger than the field in the center of the laser cavity. Figure 16 illustrates the result of assuming that the ionization rate is given by Eq. (35). Notice that the lines of constant potential are not evenly spaced in Figure 16. Comparing Figures 15 and 16 it is evident that while near the anode the lines in Figure 16 are more closely spaced, the reverse is true near the cathode. The electric field at the anode is 30-40% greater than at the cathode. This results in a 30-35% increase in the electrical energy deposited near the anode as shown in Figure 16. The highest rate of energy deposited in Figure 17 is in the region where the anode surface begins to curve. This is a result of a slight bulge in the anode boundary. Such a bulge is due to the method the computer maps the boundary and is not present in the actual cavity. Finally, the optical gain is expected to have the same topology as the electrical energy deposited.

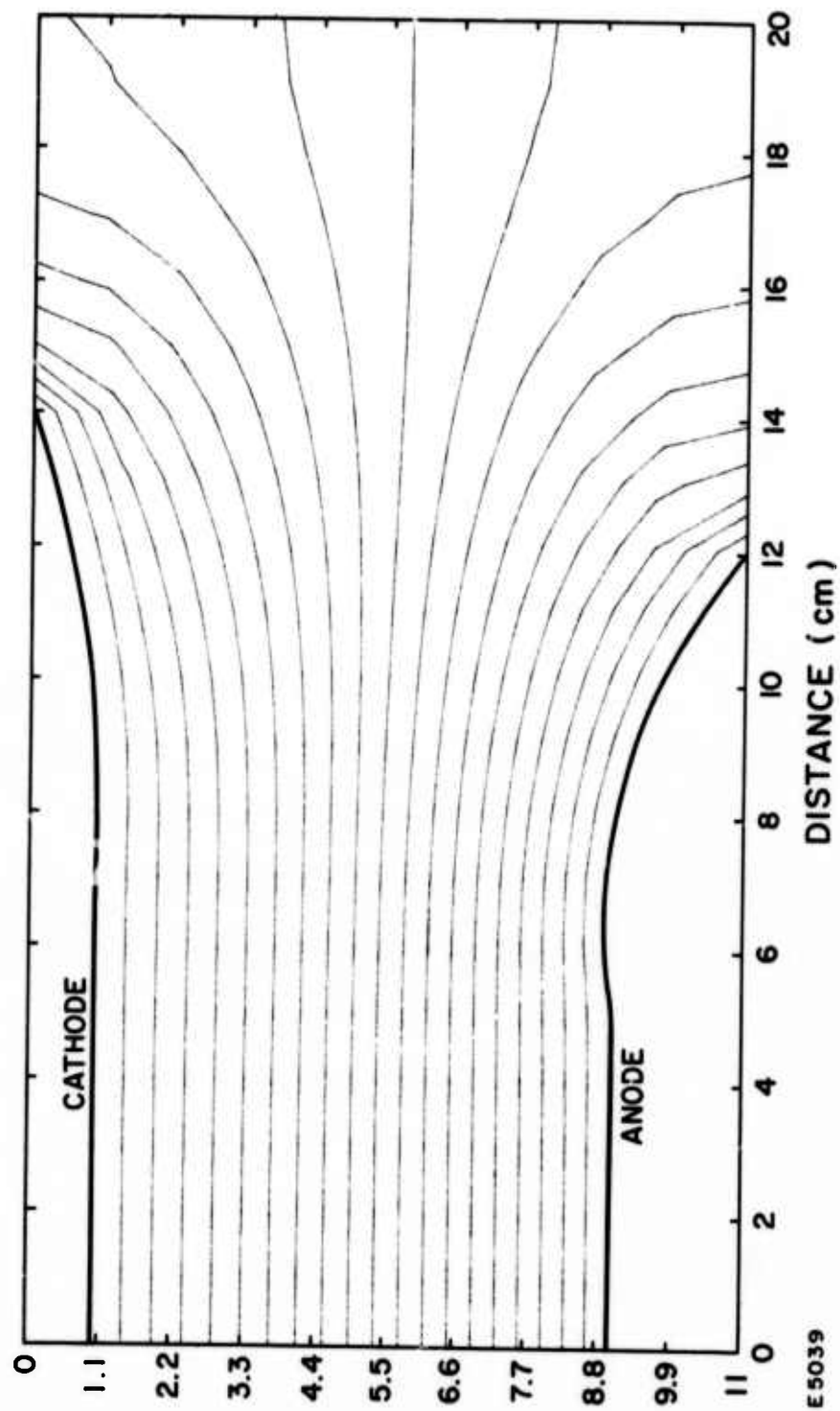


Figure 15 Potential Distribution in Cavity Neglecting Nonuniform Ionization

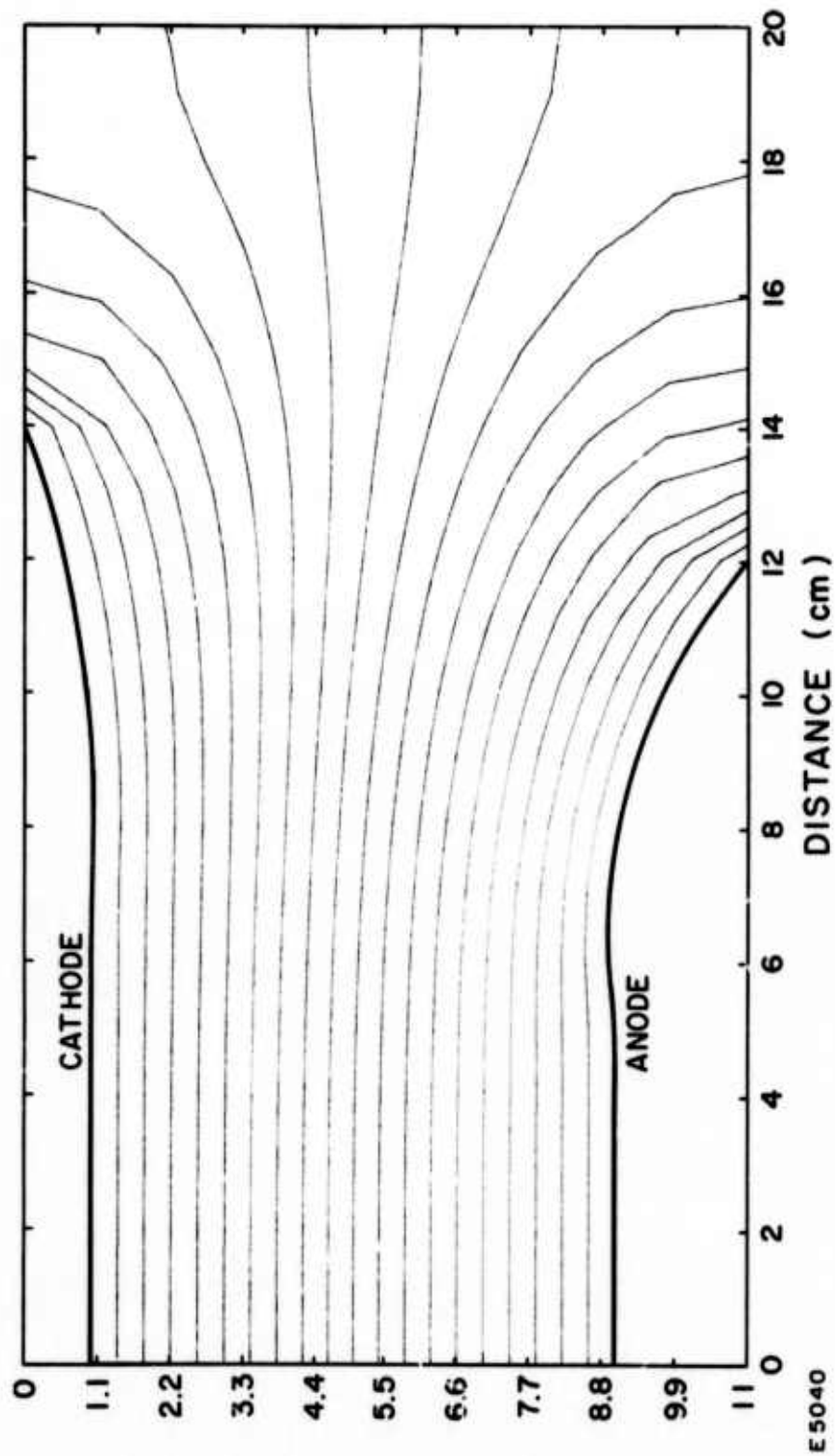


Figure 16 Potential Distribution Assuming Ionization Rate Eq. (35)

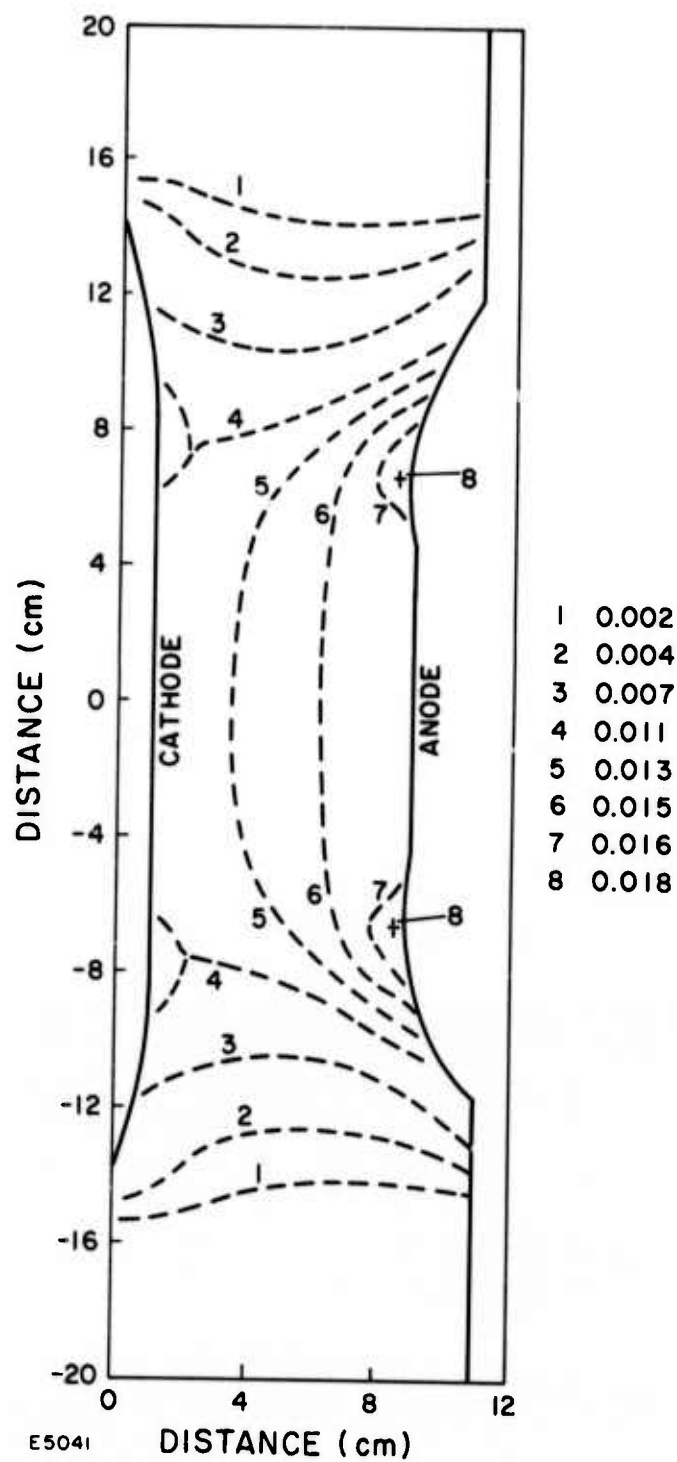


Figure 17 Distribution of Electrical Energy Deposition in Cavity. The relative electrical energy input densities are indicated in the key.

D. FABRICATION AND TESTING

The entire flow system and heat exchanger unit have been constructed, assembled and integrated. Integration with the electron gun will not take place until after the flow and homogeneity tests. The electrode system will be fabricated in the coming month and will be installed after the initial flow tests.

Before the final assembly of the heat exchanger a series of thermocouples was embedded in the central porous plate in order to measure the temperature distribution during the cooling process. Heating coils were mounted underneath the heat exchanger to allow for rapid (several hours) warmup of the system. The net mass of the heat exchanger is the order of 10^5 grams and a heat input of the order of 10^7 joules is required to regain room temperature.

Preliminary cooling tests with liquid nitrogen resulted in the development of several leaks in the liquid nitrogen manifold system. This was presumably due to the very rapid contraction and resulting mechanical strains as liquid nitrogen entered the system. To avoid this, a cooling cycle has been developed to allow the fairly uniform and initially much slower cooling of the system. Tests were then conducted with the entire system being cooled down to liquid nitrogen temperature. Thermocouple measurements indicated the maximum variation of 2°C at liquid nitrogen temperature across the entire central plate of the heat exchanger.

There is still some evidence of leaks developing at or near liquid nitrogen temperature in the manifold. These leaks only develop at very low temperature and are not apparent at room temperature. They

presumably occur due to mechanical stress in the Swagelock fittings used to construct the liquid nitrogen manifold. Although these leaks will not hold up flow testing in the immediate future, provision is being made for replacement of the Swagelock fittings with an all welded manifold to try and avoid leaks in the future.

REFERENCES

1. Center, R. E. and Caledonia, G. E., "Parametric Performance Predictions for High Power Pulsed Electric CO Lasers," Avco Everett Research Laboratory Research Report 403, to be published.
2. Lacina, W. B. and McAllister, G. L., submitted to Appl. Phys. Lett.
3. Center, R. E., IEEE J. Quantum Electron., QE-10, 208 (1974).
4. Eng, R. S., Kildal, M., Mikkelsen, J. C. and Spears, D. L., private communication and Appl. Phys. Lett. 24, 231 (1973).
5. McClatchey, R. A., ARCRL-71-0370, 1st July 1971, Environmental Research Papers No. 359.
6. Lacina, W. B., Mann, M. M. and McAllister, G. L., IEEE J Quantum Electron, QE-9, 588 (1973).
7. Center, R. E., IEEE J. Quantum Electron., QE-10, 208 (1974).
8. Treanor, C. E., Rich, J. W. and Rehm, R. G., J. Chem Phys., 48, 1728 (1968).
9. Brag, K. N. C., J. Phys. B. 1, 705 (1968).
10. Caledonia, G. E. and Center, R. E., J. Chem. Phys. 55, 552 (1971).
11. Schulz, G. J., Phys. Rev. A135, 988 (1964).
12. Boness, M. J. W. and Schulz, G. J., Phys. Rev., A8, 2883 (1973).
13. Powell, H. T., J. Chem. Phys. 59, 4937 (1973).
14. Szewczyk, A. A., "Combined Forced and Free Convection Laminar Flow," Trans. A.S.M.E. J. Heat Transfer 86, 501-507 (1964).
15. Merkin, J. H., "The Effect of Buoyancy Forces on the Boundary Layer Flow over a Semi-Infinite Vertical Flat Plate in a Uniform Free Stream," JFM 35, 439-450 (1969).
16. Lloyd, J. R. and Sparrow, E. M., "Combined Forced and Free Convection Flow on Vertical Surfaces," Int. J. Heat Mass Transfer 13, 434-438 (1970).

17. Oosthuizen, P. H. and Hart, R., "A Numerical Study of Laminar Combined Convection Flow over Flat Plates," Trans. A.S.M.E. J. Heat Transfer 95, 60-63 (1973).
18. Wilks, G., "Combined Forced and Free Convection Flow on Vertical Surfaces," Int. J. Heat Mass Transfer 16, 1958-1963 (1973).
19. Eckert, E. R. G., Heat and Mass Transfer, McGraw-Hill, New York (1959).
20. Eckert, E. R. G. and Jackson, T. W., "Analysis of Turbulent Free-Convection Boundary Layer on Flat Plate," NACA Report 1015 (1951).
21. Jacob, J. H., Reilly, J. P. and Pugh, E. R., J. Appl. Phys. 45, 2609 (1974).
22. Sockett, S. J., Lawrence Berkeley Laboratory Report #1779, January 1974.
23. Douglas-Hamilton, D. H., J. Chem. Phys. 58, 4820 (1973).
24. Center, R. E., J. Appl. Phys. 44, 3538 (1973).
25. Jacob, J. H. and Bethe, H. A., unpublished.